

Finite element simulation of two dimensional orthogonal cutting process and comparison with experiments

Master's thesis in Aerospace Engineering

Institut of Applied Mechanics, RWTH Aachen

and

Department of Aerospace Engineering, FH Aachen

- submitted by: Rex Bedzra
Master of Science in Aerospace Engineering
- First supervisor: Dr.-Ing. Ivaylo Vladimirov
Institut of Applied Mechanics, RWTH Aachen
- Second supervisor: Prof. Jörn Harder
Department of Aerospace Engineering, FH Aachen
- Third supervisor: Prof. Stefanie Reese
Institut of Applied Mechanics, RWTH Aachen
- Date of submission: August 2013

Statement of authorship

I hereby declare that this thesis is written and the work presented in it are carried out independently and no other sources have been used other than the ones stated in the reference.

Rex Bedzra

Aachen, August 2013

Summary

The integrity of the machined surface and tool life are the most important considerations during machining. To be able to achieve an optimum in machined surface integrity and to reduce tool wear which in essence means cost, it is important to have an insight into process output parameters i.e. workpiece residual stress, chip morphology, cutting force, feed force and induced temperatures that have an influence on the machinability of the material. Traditionally most of the output parameters mentioned above were determined from experiments which were time consuming and very expensive. With the advent of the finite element method coupled with advanced material models, it is possible to determine these output parameters by means of finite element simulations. This implies the number of experimental tests required in order to study the influence of these parameters on surface integrity and tool wear is greatly reduced. As a result, only a few experiments are required to validate the finite element model. The benefit of this approach is the fact that process output parameters are determined in a timely and a cheaper manner which leads to a reduction in production cost.

The focus of this thesis is to develop a finite element model of the orthogonal cutting process for Inconel 718 which is capable of predicting the aforementioned process output parameters by means of the commercial finite element software package ABAQUS/explicit. In order to check the validity of the developed model, predicted results are compared to experimental results obtained from two dimensional orthogonal cutting tests. Additionally, sensitivity analyses are carried out on the model to check the influence of mesh density, friction between workpiece and tool and workpiece thermophysical properties on predicted simulation results.

Contents

1	Introduction	1
1.1	Motivation	1
1.2	Scope and objective	2
1.3	Outline	2
2	Cutting mechanics	5
2.1	Orthogonal and oblique cutting	5
2.2	Deformation zones and shear plane	8
2.3	Analytical cutting models	9
2.3.1	Ernst and Merchant single shear plane model	11
2.3.2	Slip-line field models	14
2.3.3	Shear zone models	16
3	Finite element modeling	19
3.1	Finite element method	19
3.2	Basic concept of FEM	19
3.3	Lagrangian and Eulerian view of the continuum	21
3.4	Explicit and implicit time integration	22
3.5	Thermomechanical coupling	23
3.6	Nonlinearities	23
3.7	Solid formulation and flow formulation	24
3.8	Finite element modeling of machining	25
3.8.1	Meshing	25
3.8.2	Contact	26
3.8.3	Material modeling	27
3.8.4	Friction modeling	31
3.8.5	Modeling material separation	33
3.8.6	Adaptive meshing	37
3.8.7	Finite element software packages	38

4 Orthogonal cutting experiment and simulation	41
4.1 Orthogonal cutting experiment	41
4.1.1 Experimental setup	41
4.1.2 Forces and temperatures	43
4.1.3 Chip thickness and chip morphology	45
4.2 Simulation setup	47
4.2.1 Finite element model	48
4.2.2 Workpiece thermal model	51
4.2.3 Workpiece mechanical model	52
4.2.4 Mechanical and thermal properties of cutting tool	55
4.2.5 Friction between tool and workpiece	55
4.3 Comparison between simulation and experiment	56
4.3.1 Cutting forces and feed forces	56
4.3.2 Workpiece temperature profile	58
4.3.3 Chip thickness and chip morphology	59
4.4 Discussions	61
4.4.1 Influence of friction on predicted results	61
4.4.2 Effect of mesh density on predicted results	66
4.4.3 Parameters influencing chip serration	68
5 Conclusions	73
List of Figures	75
List of Tables	77
Bibliography	79

1 | Introduction

1.1 Motivation

Nickel based super alloy Inconel 718 (IN 718), as described in Thakur et al. [2009], has wide application in various fields of engineering, particularly where properties such as high temperature resistance, corrosion resistance, creep resistance, good ductile to brittle transition temperature during low temperature applications and high strength to weight ratio are of importance. Furthermore, It has a good yield strength (550 MPa) even at elevated temperatures (760°C). It is mostly used in gas turbine engines for the manufacture of components such as turbine blades, disks, combustion chambers, bolts, shafts, exhaust systems etc. The nominal composition of IN 718 in cast and wrought form is given in Table 1.1.

Machining of IN 718 proves a serious challenge due to its unique combination of properties such as high temperature strength, hardness, and chemical wear resistance. Although these properties are desirable design requirements, they pose a great challenge to manufacturing engineers due to the high temperature and stresses generated during machining. In machining IN 718, Rahman et al. [1997] identified two main reasons why the aforementioned difficulties arise. These are the reduction of tool life due to the work hardening and attrition properties of the alloy as well as metallurgical damage to the workpiece as a result of high cutting forces which gives rise to work hardening, surface tearing and distortion. High speed cutting of Inconel 718 results in the formation of serrated chips, see Figure 1.1. The mechanism behind this type of chip formation is not fully understood. There are mainly two theories competing for an explanation of this mechanism. The first theory states that cracks are initiated at the free surface of the workpiece which leads to chip segmentation. The second theory is based on shear localization mainly caused by thermal softening of the workpiece material (Nakayama

Table 1.1: Nominal composition of IN 718 A.S.M [1997]

	Element	Ni	Cr	Fe	Mo	Nb	Ti	Al	C	Cu
Cast Form	Weight [%]	53	19	18	3	5	0.9	0.5	0.04	0.1
Wrought Form	Weight [%]	52.5	19	18.5	3	5.1	0.9	0.5	0.08	0.15

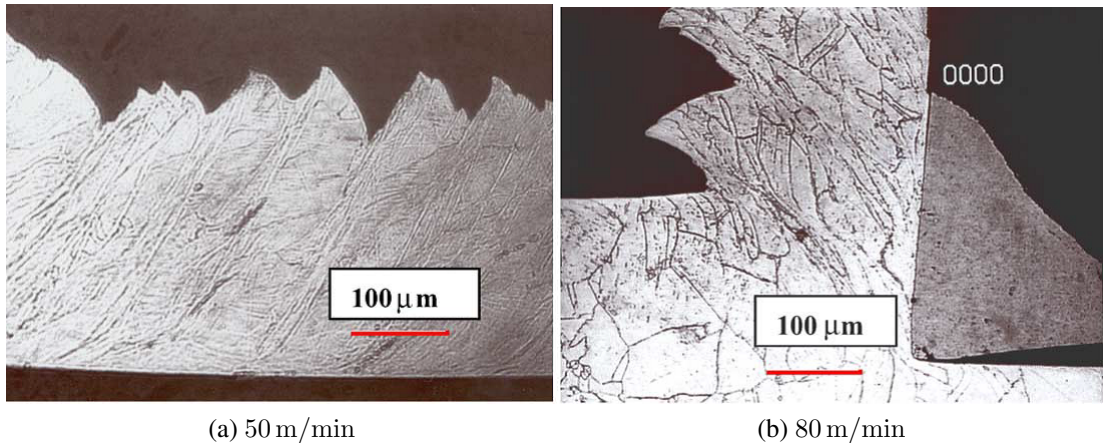


Figure 1.1: Etched chip micrographs of Inconel 718 at cutting speeds of 50 m/min and 80 m/min (Soo et al. [2004]).

et al. [1988]; M.C. Shaw [1993]).

To improve surface integrity and increase tool life, it is necessary to identify the important process output parameters which critically influence machinability. This can be done by parameter studies using finite element simulations. Once the most promising design avenues are determined, the actual alloy modification can then be undertaken. Creating a reliable computer model of the metal cutting process is the first and most crucial step in this process.

1.2 Scope and objective

The objective of this thesis is to create a finite element model, which employs a Johnson-Cook plasticity model and a Johnson-Cook damage model, to describe the two-dimensional orthogonal cutting process of Inconel 718 using the commercial finite element software package ABAQUS/explicit. The results obtained from the simulations are compared to experimental results and sensitivity analyses are carried out to check the influence of mesh density, coefficient of friction between workpiece and tool, and the thermophysical material properties of the workpiece on predicted simulation results.

1.3 Outline

The thesis is organized as follows.

In Chapter 2, the mechanics of metal cutting is discussed. In particular, orthogonal and oblique cutting processes are defined. Furthermore, the location of the deformation zones

and shear plane during orthogonal cutting is described. The types of chips typically produced during cutting are also described. Additionally, analytical cutting models such as the Ernst and Merchant single shear plane model, slip-line field models and shear zone models for calculating the minimum required cutting force is discussed.

Chapter 3 gives a basic overview of the finite element method i.e. the Langrangian and Eulerian view of the continuum, types of interpolation functions, element material properties, assembly of the element equations, explicit and implicit solution schemes, thermomechanical coupling etc. Additionally, the step by step application of the finite element method to machining, which entails tool and workpiece meshing, contact modeling, material modeling, friction modeling, material separation as a result of cutting, adaptive remeshing and commercial finite element software packages, is discussed.

Chapter 4 discusses the experimental setup, the experimentally obtained cutting forces, feed forces, workpiece temperature profile, chip thicknesses and chip morphologies. Additionally, aspects of the corresponding finite element model such as tool and workpiece mesh, element types, contact modeling, thermal and mechanical model of workpiece and tool, material models, damage model and friction modeling between tool and workpiece are described. Also model predicted process output parameters such as cutting forces, feed forces, workpiece temperature distribution profile, chip thicknesses and chip morphologies are compared to their corresponding experimental results. Furthermore, the effect of mesh density, coefficient of friction and thermophysical material properties on process output parameters is discussed.

As a conclusion, the last chapter gives a summary of the obtained results as well as possible ways by which the model can further be improved.

2 | Cutting mechanics

If not explicitly stated, most of the information in here is obtained from Markopoulos [2013].

The initial objective of studying and modeling metal machining is to provide a theory which leads to the prediction of cutting performance and thus solve practical problems confronting industry. The first analytical models set the bases for more advanced methods such as the finite element method developed later in the course of time when the tools for realistic computation cost and analyses time became available with computer advances. With the availability of commercial finite element software, this method has proven to be the favorite modeling tool for researchers in the field. This is evident by the large number of publications on this subject and by the fact that there is commercial finite element software solely for the purpose of modeling machining.

2.1 Orthogonal and oblique cutting

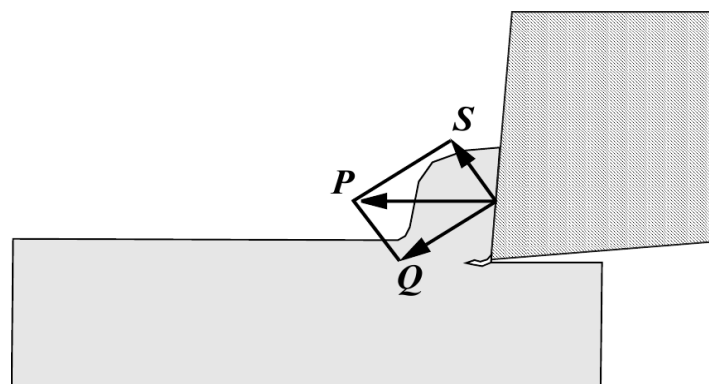


Figure 2.1: Interaction between tool rake face and chip (Kalhorri [2001]).

Metal cutting is a process whereby two components are arranged together and one component applies an external force on the other causing fracture of the other as illustrated in Figure 2.1. This fracture is due to an external force P which decomposes into a bending stress S and a shear stress Q due to compression. The chip flow as a result of the metal cutting process by all

wedged tools can be described in theory by two different cutting schemes termed orthogonal and oblique cutting.

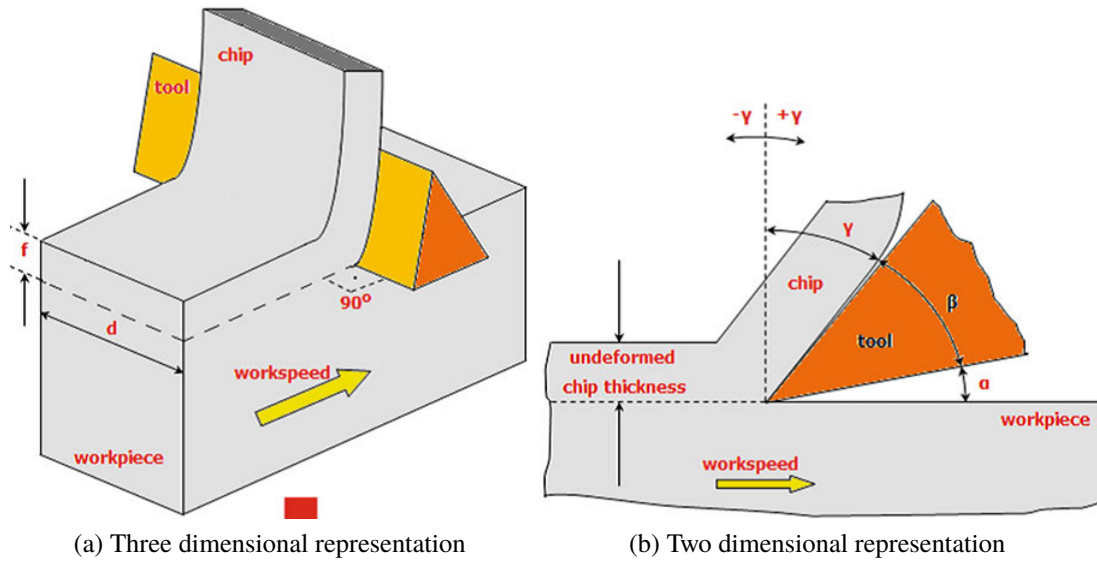


Figure 2.2: Orthogonal cutting depiction (Markopoulos [2013]).

Orthogonal cutting represents a two dimensional mechanical problem with no side curling of the chip. It represents only a small fragment of machining processes such as planning, end turning of a tube and helical orthogonal cutting. However, it is widely used in theoretical and experimental work due to its simplicity. Because of its two dimensional nature, many independent variables are eliminated such as a third force component leaving only the cutting force and the feed force. The cutting edge of the tool in an orthogonal cutting process is perpendicular to the direction of relative motion of the workpiece as depicted in Figure 2.2a. From the relative movement of the workpiece and the cutting tool, a layer of material in the form of chip is removed. In order to continue the removal of material, the tool is taken to its starting point and fed downwards by an amount f called the feed. Perpendicular to the feed is the depth of cut depicted in Figure 2.2a as d , which can be smaller or equal to the width of the tool edge. The surface along which the chip flows is the rake face and a line perpendicular to the machined surface is called the rake angle denoted by γ . The face of the tool that is near the machined surface of the workpiece is the flank face. The angle between the flank face of the tool and the workpiece is called the clearance angle depicted by α . The depiction of the rake angle γ in Figure 2.2b is positive. For a negative rake angle, the tool rake face is more into the direction of chip flow and causes the wedge angle β to increase, see Figure 2.2b. For ductile materials, a positive rake angle is preferred since this result in a reduced wedge angle which implies a weaker tool. For high-strength materials, such as nickel-based

alloys, a zero rake angle or a negative rake angle is preferred since this leads to an increase in wedge angle which implies a stronger cutting edge. However, a stronger cutting edge has the disadvantage of requiring greater power consumption and needing a robust tool-workpiece setup to compensate for vibrations. The flank face of the tool does not participate in chip removal but ensures the tool does not rub on the newly machined surface thus affect surface quality. However, the clearance angle affects the cutting tool wear rate. If the tool clearance angle is too large, it will reduce the wedge angle of the tool and lead to a weaker tool. On the other hand, if the tool clearance angle is too small, it will turn to rub on the machined surface.

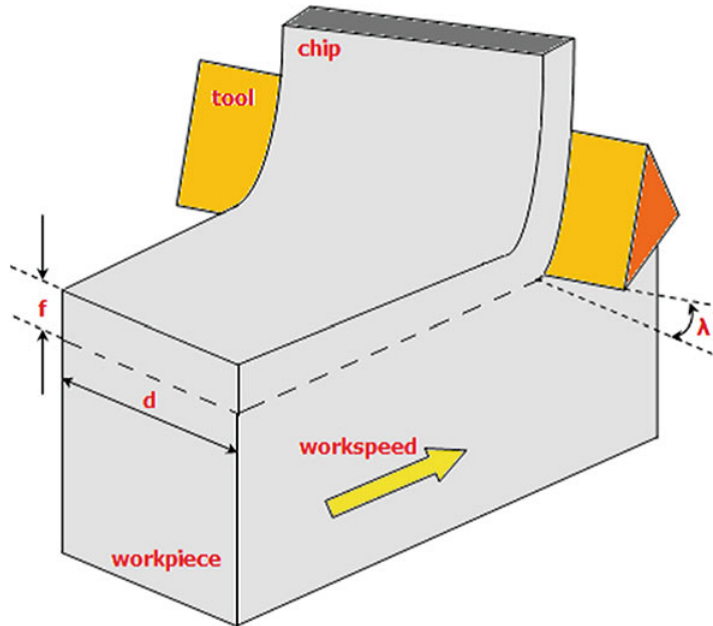


Figure 2.3: Oblique cutting depiction (Markopoulos [2013]).

Oblique cutting is a more general case of cutting compared to orthogonal cutting. In this type of cutting, the cutting tool is inclined at an angle λ as shown in Figure 2.3. It corresponds to a three dimensional problem with a more realistic chip flow representation and a more complex analysis due to the presence of three force components and the curling of the chip. The three force components are cutting force, feed force and back force, with the cutting force usually being the largest. For orthogonal cutting, the back force is ignored and the force system lies in a single plane which is normal to the tool cutting edge. The measurement or theoretical calculation of the cutting force and the feed force as well as their resultant force has been the subject of numerous researchers in the past. The prior knowledge of cutting forces before the commencement of cut, if possible, is important to estimate the power requirements of the machine tool, the cutting tool properties and the quality of cut. For example, if the feed force is high and the tool holder is not stiff enough, the cutting edge will be pushed away from the

workpiece surface, causing lack of dimensional accuracy. Furthermore, the determination of cutting forces can easily lead to the calculation of other parameters such as stresses.

2.2 Deformation zones and shear plane

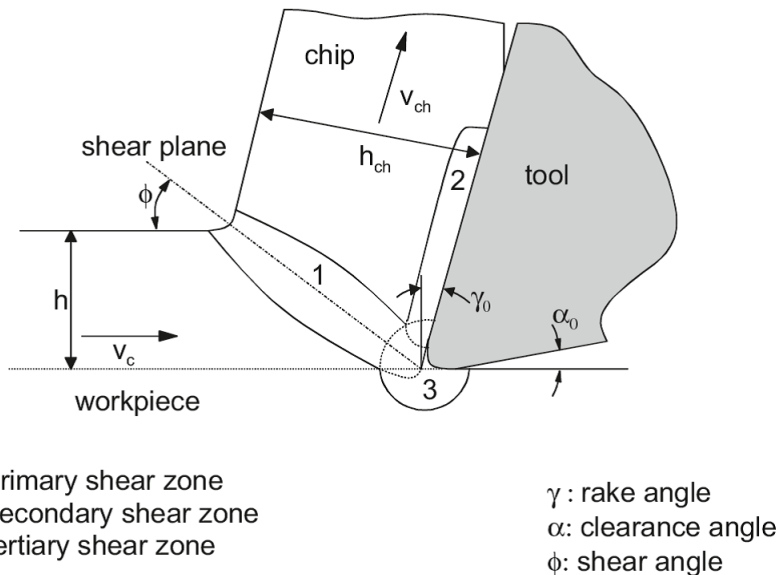


Figure 2.4: Locations of the deformation zones in two dimensional orthogonal cutting (Tönshoff [1995]).

There are generally three distinguishable deformation zones in machining, namely the primary shear zone, secondary shear zone and tertiary shear zone, see Figure 2.4. The primary deformation zone is indicated by region 1. The workpiece material crossing the lower border of this region undergoes large deformations at high strain rates and exits the zone at the upper border of the region, work hardened. It is determined by microscopic examination and experiments that chips are produced by shear within this zone. The secondary deformation zone which is known as the sliding region is indicated in Figure 2.4 by 2. Along the boundary of this region which is located between the rake face of the tool and the chip, the material is deformed due to intensive interfacial friction. The tertiary region indicated by the zone 3 is known as the sticking region here material adheres to the tool and as a result shear within the chip is observed. All three deformation zones are characterized by temperature rise due to severe plastic deformation in the primary and tertiary zone and due to friction in the secondary zone. Furthermore high cutting speeds do not allow heat to be conducted and heat is concentrated at a small area around the cutting tool edge. Strain hardening due to deformation and softening due to temperature alter the chip formation characteristics in all steps of its formation.

Shearing in the primary deformation zone takes place along a shear plane, characterized by shear angle ϕ , between the shear plane and the workpiece surface. Although this single shear plane model is criticized, it is usually referred in machining handbooks due to its simplicity and it is the basis for calculating several process parameters. In any case, it is of vital importance to estimate shear angle and friction parameters in order to calculate cutting forces. In the next section we will see how the determination of the shear angle helps in the determination of the parameters stated above from analytical cutting models.

Depending on the cutting condition and workpiece material, different kinds of chips may be produced as depicted in Figure 2.5. The three basic types of chips that are typically encountered in metal cutting are continuous chips, continuous chips with built-up edge (BUE) and discontinuous chips. However, besides these basic chip types, another chip type named segmented or serrated chip is observed. This was documented later because it mainly occurs at higher cutting speeds and when machining difficult to machine materials such as Nickel-based superalloys. Continuous chip is observed when cutting ductile materials at high speeds. The chip is detached from the workpiece through shearing in the primary deformation zone. The sheared chip slides onto the tool face, precisely the secondary deformation zone and is further deformed. Although continuous chips are associated with low cutting forces, long chips or curling of the chips are not desirable as they turn to cause handling problems and removal problems in practical operations. To avoid this, tools with chip breakers are employed in machining such materials. Under conditions of low cutting speeds where the friction between the chip and the rake face of the tool is high, the chip may be welded to the tool face. This accumulation of chip material is known as BUE. Discontinuous chips are formed when machining brittle materials or ductile materials at very low speeds due to severe strains encountered during the process. As a result, the chip breaks into small pieces in the primary deformation zone during the chip formation process. The last type of chip which is the shear localized chip or the serrated chip is formed as a result of flow stress reduction due to temperature increase. Under the proper conditions, rapidly heated material in a narrow band in front of the tool can become much weaker than the surrounding material, leading to localized deformation.

2.3 Analytical cutting models

The earlier analytical models of the cutting process are considered the predecessors of numerical models. Over the course of time, various models have been proposed for predicting cutting forces. Some of these models include shear plane model, slip-line field model and shear zone

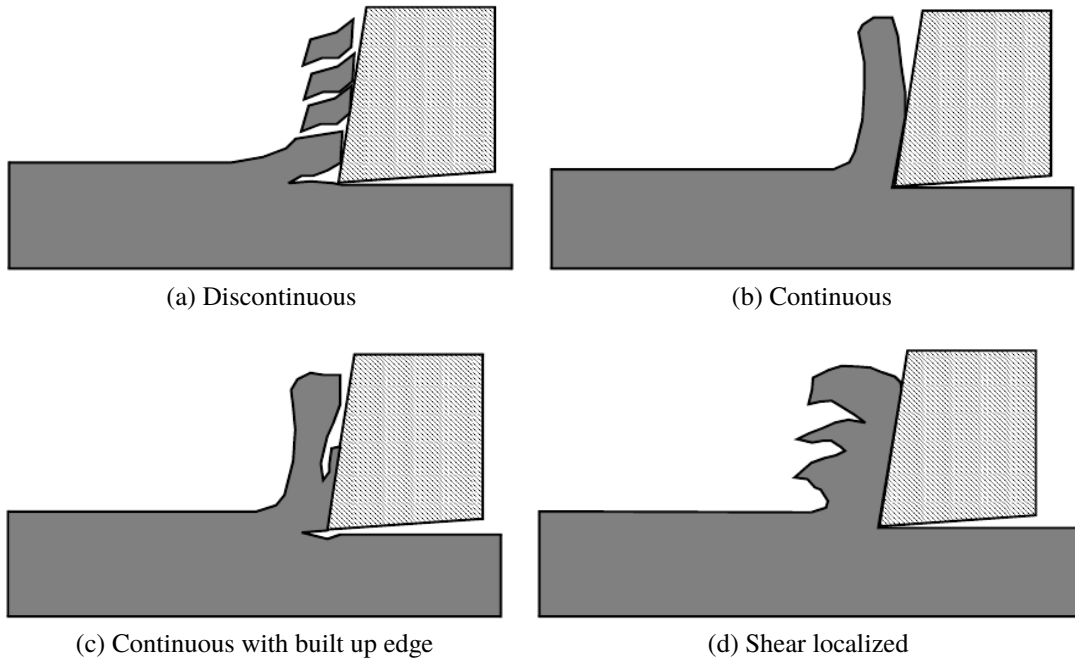


Figure 2.5: Types of chips produced in metal cutting (Kalhorri [2001]).

model. In this section, a short review is done on some of these analytical models.

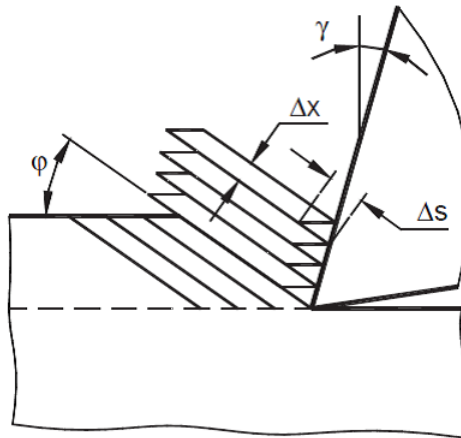


Figure 2.6: Piispanen's deck of cards model (V.Piispanen [1948]).

V.Piispanen [1948] published a work in which he applied a pack of cards analogy to explain the deformation pattern during chip formation process. As shown in Figure 2.6, the chip formation process is represented by a deck of cards inclined at an angle φ to the cutting direction. As the tool moves relative to the workpiece, it engages one card at a time causing it to slide over its neighbor. Each chip segment (each card) is represented by a small thin

parallelogram. Slipping occurs between each chip segment along the shear plane. V.Piispanen [1948] made the following assumptions:

- The shear action occurs on a perfectly plane surface.
- The inhomogeneity of strain is exaggerated.
- Chip curl is not accounted for in the model.
- Assumption of no built up edges as would normally be encountered during machining.
- Tool face friction is assumed to cause only elastic deformation rather than plastic deformation.

In spite of its simplicity and its limitations, this analogy of the chip formation process presented a good illustration of how shearing action during machining occurs. Based on this model a quantitative model was later derived by Ernst and Merchant [1941].

2.3.1 Ernst and Merchant single shear plane model

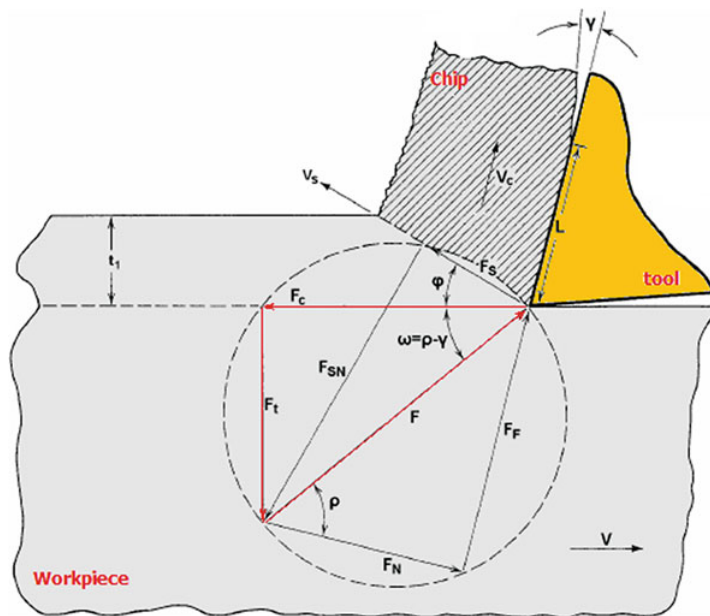


Figure 2.7: Illustration of Merchant's circle (Markopoulos [2013]).

The first quantitative analysis of the cutting force based on the upper bound theory was developed by Ernst and Merchant [1941]. Ernst and Merchant [1941] assumed the chip was formed by shear action along a single plane inclined at an angle φ . The chip is straight and

has infinite contact length with the tool. The shear stress along the shear plane is equal to the material flow stress in shear. The chip is assumed to be a rigid in equilibrium. Equilibrium refers to the forces acting on the chip-tool interface and across the shear plane. In Figure 2.7, the Merchant's circle force diagram is given. All forces shown act at the tool tip.

The resultant force F is resolved into components F_N normal to the tool face and F_F along the direction of the tool face. It is also resolved into F_{SN} and F_S that are normal to and along the shear plane, respectively. Finally, it is also resolved into components F_c and F_t which stands for the cutting force and the feed force, respectively. Furthermore, the rake angle γ , shear angle φ and the mean friction angle between chip and tool ρ are shown. The friction angle ρ is related to the coefficient of friction μ through

$$\rho = \tan \mu = \tan \left(\frac{F_F}{F_N} \right). \quad (2.1)$$

According to the theory of Ernst and Merchant [1941], which is a minimum energy principle, a shear angle needs to be found to ensure the cutting work reduces to a minimum. In other words, since the work is proportional to the cutting force F_c , an expression of the cutting force with the shear angle φ needs to be found for which F_c is a minimum. From Figure 2.7, it can easily be concluded that

$$F_S = F \cos (\varphi + \rho - \gamma). \quad (2.2)$$

Furthermore, the same force component can be calculated in relation to the shear strength of the workpiece material on the shear plane τ_S , the cross sectional area of the shear plane A_S and the cross sectional area of the undeformed chip A_C , via

$$F_S = \tau_S A_S = \tau_S \frac{A_C}{\sin \varphi}. \quad (2.3)$$

Thus from equation (2.2) and (2.3) the resultant force F is obtained as

$$F = \frac{\tau_S A_C}{\sin \varphi} \left(\frac{1}{\cos (\varphi + \rho - \gamma)} \right). \quad (2.4)$$

Furthermore F_c can be related to F as

$$F_c = F \cos (\rho - \gamma). \quad (2.5)$$

A combination of equations (2.4) and (2.5) leads to

$$F_c = \frac{\tau_s A_C}{\sin \varphi} \left(\frac{\cos(\rho - \gamma)}{\cos(\varphi + \rho - \gamma)} \right). \quad (2.6)$$

Differentiating equation (2.6) with respect to φ and equating it to zero, the following expression is obtained

$$\frac{\cos \varphi}{\sin \varphi} = \frac{\sin(\varphi + \rho - \gamma)}{\cos(\varphi + \rho - \gamma)}. \quad (2.7)$$

By employing the trigonometrical identities $\cos \varphi = \sin(\pi/2 - \varphi)$ and $\sin \varphi = \cos(\pi/2 - \varphi)$, the following relation is obtained

$$\frac{\pi}{2} - 2\varphi = \rho - \gamma. \quad (2.8)$$

Equation (2.8) gives the possibility to calculate a shear angle which results in a minimum cutting force. This equation agreed poorly with experimental results. Merchant [1945] attempted an alternative solution in which deformation and friction are reflected through a change of the force acting in the direction perpendicular to the shear plane. As a result, the normal stress σ_{SN} acting on the shear plane is related to the shear stress τ_s through the following relation

$$\tau_s = \tau_0 + k\sigma_{SN}. \quad (2.9)$$

This relation is known as the Bridgman relation and is analogous to the equation of a line where k is the gradient and τ_0 is the τ_s intercept. From Figure 2.7, it can easily be concluded that

$$F_{SN} = F \sin(\varphi + \rho - \gamma). \quad (2.10)$$

Substituting (2.2) into (2.10) and dividing through by the area of the shear plane A_S results in

$$\sigma_{SN} = \tau_s \tan(\varphi + \rho - \gamma). \quad (2.11)$$

Furthermore substituting (2.11) into (2.9) and the result into (2.4), the resultant force force F is obtained as

$$F = \frac{\tau_0 A_C}{\sin \varphi (1 - k \tan(\varphi + \rho - \gamma))} \left(\frac{1}{\cos(\varphi + \rho - \gamma)} \right). \quad (2.12)$$

Substituting (2.12) into (2.5), the cutting force F_c is obtained as

$$F_c = \frac{\tau_0 A_C}{\sin \varphi (1 - k \tan (\varphi + \rho - \gamma))} \left(\frac{\cos (\rho - \gamma)}{\cos (\varphi + \rho - \gamma)} \right). \quad (2.13)$$

By proceeding in a similar manner as earlier and differentiating (2.13) with respect to φ and equating it to zero, a new relation for the shear angle is obtained as

$$2\varphi + \rho - \gamma = \tan k. \quad (2.14)$$

According to Astakhov [2005], there is still a marked disagreement between the new solution and experimental results.

2.3.2 Slip-line field models

Ernst and Merchant [1941] did not consider the state of stress and strain in the workpiece material ahead of the tool, in the chip and at the tool/chip interface. The first attempt to apply simplified plasticity analysis such as slip-line field theory to metal cutting, more specifically to orthogonal cutting with continuous chip, was made by Lee and Schaffer [1951].

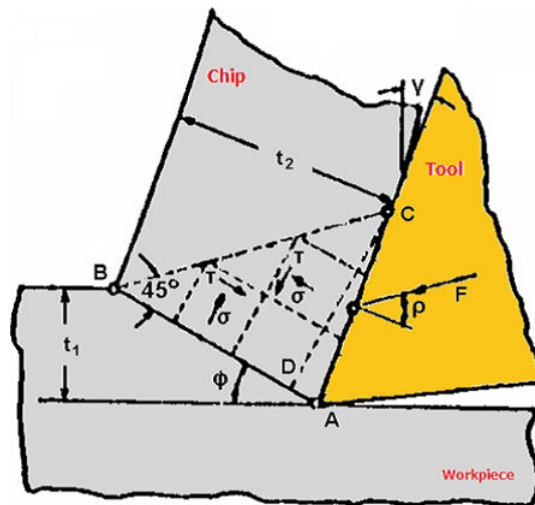


Figure 2.8: Illustration of Lee and Shaffer's slip-line theory for orthogonal cutting (Markopoulos [2013]).

In order to construct a slip-line field which describes a particular problem, certain rules according to the slip-line theory must be adhered to. The first of which is the fact that the boundary of a material that is plastically loaded and another that has not yet yielded is a slip-line. In machining, the border of the primary deformation zone with the workpiece on

one side and the chip on the other side are slip-lines. Secondly, slip-lines must intersect free surfaces at an angle of 45° .

Lee and Schaffer [1951] assumed that in this plane strain condition, the workpiece material is rigid perfectly plastic, i.e. the elastic strain is neglected during deformation and once the yield stress is exceeded, deformation takes place at a constant stress varying strains, strain rates and temperatures. The constructed slip-line is shown in Figure 2.8. In this lower bound solution, all deformations take place in a stress field bounded by rigid bodies. This stress field transmits the cutting forces from the shear plane to the chip resulting in the triangular plastic zone ABC. In this region, no deformation occurs but the material is stressed to its yield point, where the maximum stress is the shear stress on the shear plane. The two directions of the maximum shear stress are indicated by the slip-lines. The shear plane AB is also a slip-line because the maximum shear stress occurs along the shear plane. Furthermore, BC can be regarded as a free surface since no forces act on the chip after the boundary BC, stresses can not be transmitted from there. Thus according to the rules of constructing a slip-line, angle ABC is equal to $\pi/4$. Assuming stresses act uniformly at the tool/chip interface, normal stresses will meet the boundary at angles ρ which means the angle ACB is $\pi/2 - \rho$. The shear angle can then be calculated by summing the internal angles of the triangle and equating the results to π . If this is done, the following relation is obtained

$$\varphi + \rho - \gamma = \frac{\pi}{4} \quad (2.15)$$

It is evident that when the mean angles of friction between chip and tool is $\rho = \pi/4$ and the rake angle $\gamma = 0$, the shear plane angle $\varphi = 0$, which should not be possible. Lee and Shaffer proposed a solution for this case of high friction and low rake angle, assuming built up edge formation. The slip-line theory was used by other researchers who suggested curved AB and CD boundaries, see Kudo [1965]; Dewhurst [1978]. They realized different chip shapes and thickness resulted from the same specified conditions. The non-uniqueness of the possible solutions is a significant limitation, resulting mainly from the rigid plastic workpiece material assumption.

Another author who also applied the slip-line theory in the analysis of the orthogonal cutting problem was Zorev [1966]. The difference between the work of Zorev [1966] and Lee and Schaffer [1951] is that instead of a single shear plane, an approximate number of shear lines in the plastic zone, as shown in Figure 2.9a, is proposed. This is a qualitative model for which no solution is provided. This is due to the fact that the boundaries of the deformation zones are not set and thus cannot be defined (there is no steady-state mode of deformation in metal cutting

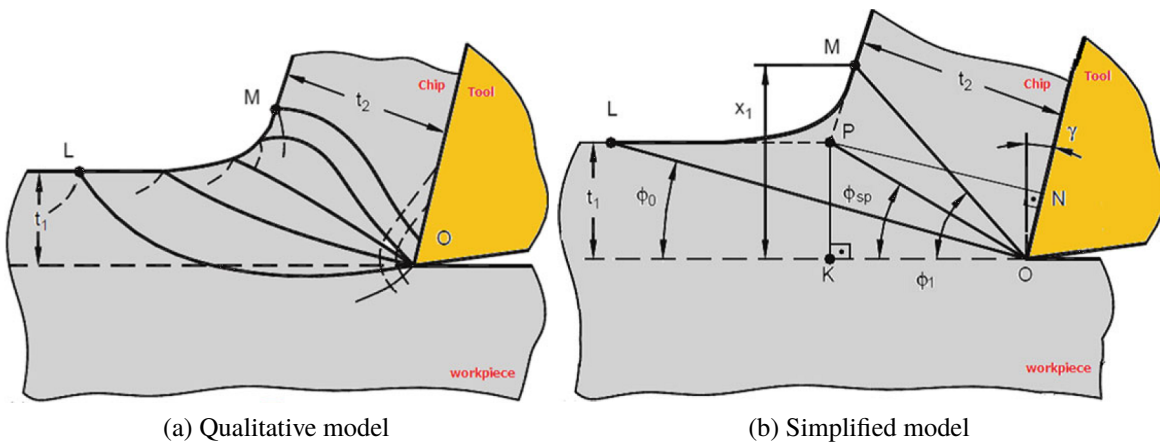


Figure 2.9: Zerov's qualitative model on the left and simplified model on the right (Markopoulos [2013]).

as the shape of the deformation zone is ever changing). Furthermore, the stress components in the deformation zone do not change in proportion to one another. However, as shown in Figure 2.9b, a simplified model was proposed. In this model, the curved shear lines are replaced by straight lines and it is assumed shearing occurs along the shear lines adjacent to the tool rake face. By using geometrical relations, a generalized relation is derived as

$$2\phi_{sp} + \rho - \gamma \approx \frac{\pi}{2} - \varphi_{sp}. \quad (2.16)$$

In this equation ϕ_{sp} is introduced, this is known as the specific shear angle and φ_{sp} is the angle of inclination of the tangent to the outer boundary of the plastic zone. The interesting thing about this solution is that if various values of φ_{sp} are substituted, the shear angle relations by other researchers are derived. For $\varphi_{sp} = 0$, the Ernst and Merchant solution is obtained. Also for $\varphi_{sp} = \pi/2 - \tan k$, the modified Merchant solution is obtained and for $\varphi_{sp} = \rho - \gamma$, the Lee and Shaffer solution is obtained.

2.3.3 Shear zone models

The next step in analytical modeling was to enhance some features that were neglected or simplified in previous models but play an important role in metal cutting. Most shear plane models assume the shear stress on the shear plane is uniform, no strain hardening and friction along the tool-chip interface is characterized by a constant friction coefficient. The last assumption is in contradiction with experimental data. By assuming the deformation takes place in a narrow band along the shear plane, more general analytical models can be derived.

The effect of yield stress varying with strain and sometimes with strain rate and temperature were considered by Oxley [1989]. Based on experimental data, where the plastic flow patterns are observed, Oxley [1989] assumed the shear zone thickness was about one tenth of the shear zone length. As a result of the aforementioned assumption, the strain rate and the strain at every point in the primary deformation zone could be calculated. The strain rates were derived from variations in the velocity with respect to position and the strains were calculated by integrating the strain rates with respect to time along the streamlines of the flow. Similar assumptions were made in order to calculate the strain rates and the strains in the secondary deformation zone.

The shear zone models are obvious improvements over the preceding models due to their complexity. Many additions to the first model proposed by Oxley [1989] are reported in the literature. A full account of these developments is out of the scope of this thesis.

3 | Finite element modeling

If not explicitly stated, most of the information here is obtained from Messner [2006] and Markopoulos [2013].

3.1 Finite element method

Many analytical models proposed in the literature do not take into account strain hardening of the workpiece material. Additionally, temperature increment in the deformation zones due to plastic deformation and friction which results in material softening is not also taken into account. This means any proper model of the metal cutting process must be capable of dealing with a coupled mechanical (plasticity) and heat transfer problem. The finite element method (FEM) is capable of performing such coupled analyses.

The finite element method is a solution method for the approximate solution of field problems. Such field problems are mathematical problems which allow the description of a continuum by means of partial differential equations with temporal and spatial dependence. Within a body, the field variables such as the stress and temperature are a function of every generic point. Consequently, mathematical problems of this kind contain an infinite number of unknowns Huebner and Thornton [1982].

3.2 Basic concept of FEM

The basic principle of the finite element method is the division of a continuum into a finite number of discrete and interdependent problems. A finite element analysis generally incorporates the following steps (Huebner and Thornton [1982]; Reddy [1993]; Zienkiewicz and Taylor [2000]):

Discretization of the continuum. During the discretization of the continuum, the domain of the solution (e.g. the workpiece in a manufacturing process) is divided into a finite number of subdomains. These subdomains are called finite elements. The geometrical shape of the applied elements depends on the nature of the problem. Table 3.1 gives an overview of common

Table 3.1: Overview of common element shapes, the corresponding nodal position and the degree of the shape function (Knothe and Wessels [1992]).

<i>geometry / type of shape function</i>	<i>one dimensional</i>	<i>two dimensional</i>	<i>three dimensional</i>
1. rectangle / linear	—•—	□	■
2. general quadrilateral / linear		◇	◆
3. rectangle / quadratic	—•—	□•□	■•■
4. curved quadrilateral / quadratic	—•—	◊	◆◆◆
5. triangle / linear		△	◆◆
6. triangle / quadratic		△•△	◆•◆
7. curved triangle / quadratic		◊	◆◆◆

element shapes. In Figure 3.1, an example for the discretization of a geometry that results in a faceted finite element mesh is given. The discretization already introduces an error due to the deviation between the actual object boundary and the boundary of the finite element mesh.

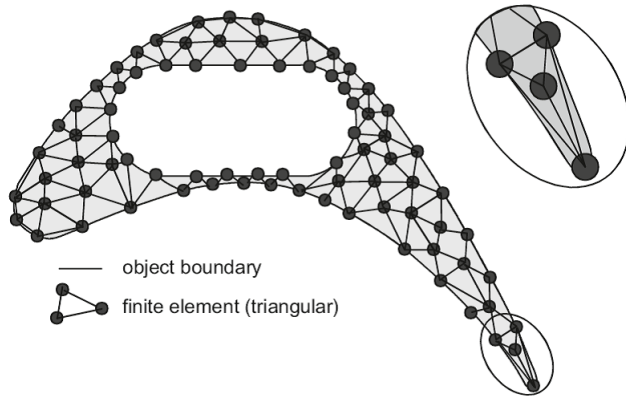


Figure 3.1: Example of a two dimensional finite element mesh with linear triangular elements, discretization of a turbine blade Huebner and Thornton [1982].

Selection of interpolation function. Now that the geometrical properties of the element have been determined, nodes and interpolation functions have to be assigned to the elements. The interpolation functions determine how the field variables are interpolated within each single element. Usually, polynomials are used to perform this task and the nodes are used as pivots

of the respective polynomial. Depending on the selected element type, the degree of the polynomial that is utilized for interpolation purposes may vary (see Table 3.1).

Determination of the element material properties. Subsequent to the discretization of the domain and the selection of the interpolation functions, the element material properties have to be determined. They describe the behavior of the element from a physical point of view. In other words, the element properties represent the link between the primary unknowns of the system (e.g. displacements) and the secondary unknowns (e.g. stresses). A common approach to obtain the element properties is performing experimental tests to determine the variation of strain against stress (stress-strain curve) and to derive a function to fit the obtained curve.

Assembly of the element equations. To find the complete influence of each of the element on the entire continuum, the matrix equations of the elements are combined to form the matrix equations of the system. The assembly procedure relies on the fact that the field variables at the common nodes of adjacent elements have the same value.

Solution of the system of equations. The set of simultaneous equations resulting from the assembly process is solved numerically to obtain the field variables. This process involves the application of numerical integration procedures which require the evaluation of integrals at discrete points within the element known as integration points. A common numerical integration scheme is the Gaussian quadrature (Zienkiewicz and Taylor [2000]). The field variables are calculated at the integration points and interpolated to other locations within the element as required.

3.3 Lagrangian and Eulerian view of the continuum

The discretization of the continuum can be based on various approaches. The most common views of the continuum are the Lagrangian and the Eulerian, Bathe [1996].

The Lagrangian view assumes the nodes of an element move with the continuum. Travelling on a node, a spectator would observe the change of the state variables of a single particle during the examined physical process. A disadvantage of the Lagrangian approach is the distortion of the finite element mesh during large displacements within the continuum. Large plastic deformations of the continuum as they occur in metal cutting require an appropriate frequent regeneration of the finite element mesh. This procedure is called remeshing. Subsequent to the generation of a new mesh, a complete remeshing cycle requires interpolation of all state variables from the old mesh to the newly generated mesh.

The Eulerian view assumes the particles of the continuum move through a fixed mesh. A spectator on a node of an Eulerian mesh would observe the states of all particles that pass his

position. This approach is particularly suitable for the analysis of stationary processes and is frequently applied in the area of fluid mechanics.

The Arbitrary Lagrangian Eulerian (ALE) approach is increasingly becoming of interest for large deformation problems and is emerging as an alternative to the two previously mentioned approaches. This approach represents a combination of both the Langrangian and Eulerian approach and neither requires the mesh to adhere to the material nor be fixed in space. Independent of the material movement, the mesh is continually moved in order to maintain an optimal element shape (Kobayashi et al. [1989]; Bayoumi and Gadala [2004]). As a result, an ALE mesh is less distorted and more regular than a Langrangian mesh. While the ALE approach is promising, it is still subject to development within commercial codes.

A Langrangian approach is chosen for the machining simulation performed in this thesis work. The advantage of the Langrangian approach is the fact that chip geometry is a result of the simulation whereas the Eulerian approach requires predefined initial chip geometry.

3.4 Explicit and implicit time integration

Many FEM codes designed to handle large plastic deformation utilize an implicit time integration scheme whereas codes that are tailored towards highly dynamic processes use explicit integration schemes.

Explicit integration schemes treat the examined physical process as a dynamic problem which can be divided into time steps. The unknowns at time $t + \Delta t$ are calculated from known quantities at time t . In most cases, the central difference scheme is used for that purpose. The scheme is stable, if the time step Δt is smaller than the time required for an elastic wave to travel through a distance corresponding to the smallest element edge length in the model. In other words, the largest possible time step depends on the speed of sound within the respective material. For solids, the speed of sound can be calculated using

$$c = \sqrt{\frac{E}{\rho}}. \quad (3.1)$$

Consequently, the maximum time step possible depends on the modulus of elasticity E and the density ρ of the material. The resulting time step can be in the range of microseconds which can lead to a large number of calculation steps. By artificially increasing the material density, which is often referred to as “mass-scaling” or artificially reducing process time, the user can increase the possible step size and thereby reduce computation time. Mass effects caused by such manipulations have to be properly compensated in order to maintain the validity of the

simulation results (Chung et al. [1998]).

Implicit schemes are not subjected to the limitations mentioned above. Implicit solvers are designed to determine the solution at time $t + \Delta t$ considering the values of the unknown quantity at time t and at time $t + \Delta t$ (Huebner and Thornton [1982]). This requires the solution of a non-linear system of equations by means of iterative methods such as the Newton-Raphson algorithm. Compared to the explicit schemes, the time step can be increased by a factor of up to 1000. However, the iterative solution of the nonlinear system of equations is time consuming (Zienkiewicz and Taylor [2000]) and mass effects are neglected.

3.5 Thermomechanical coupling

Machining processes involve large deformations at high rates. The dissipation of plastic and frictional work within real machining processes leads to a change of the temperature field within the tool and the workpiece. Mechanical and thermal calculations have to be coupled in order to account for thermal processes during a large deformation analysis. In metal cutting, this allows not only the calculation of tool and workpiece temperatures but also to enable the influence of temperature on the properties of the material to be taken into account.

The thermal and the mechanical calculations can either be performed simultaneously or conducted in a staggered approach. A simultaneous calculation requires the solution of a fully coupled system of equations for both, the mechanical and the thermal process. The more common approach is the staggered approach which relies on a purely mechanical calculation which is followed by a thermal calculation that allows the determination of the material properties under the respective conditions. The determined material properties represent the input for the next mechanical calculation step.

3.6 Nonlinearities

Generally, problems involving a linear dependence between the applied loads and the system response are referred to as linear problems. However, from a physical point of view, every real system is nonlinear but these nonlinearities can be neglected in some cases. The analysis of large deformation processes like metal cutting does not allow for one to neglect these nonlinearities. Nonlinearities can be divided into three categories:

- Material nonlinearities
- Geometric nonlinearities

- Boundary nonlinearities

The term material nonlinearities refers to problems with a nonlinear stress strain relationship as can be observed when the elastic limit of a material is exceeded and the material deforms plastically.

Geometrical nonlinearities occur in large deformation problems. A simple example is the large deformation of a beam during which the change of the beams geometry due to large deformations has significant influence on the further deformation of the beam.

Boundary nonlinearities can be observed in problems that involve changes of the contact situation between two objects or changes of the external loading conditions.

Manufacturing processes, such as metal machining, usually involves all three forms of nonlinearities. The ability of the FEM to handle all these nonlinearities makes it the preferred method for the analysis of the metal cutting process.

3.7 Solid formulation and flow formulation

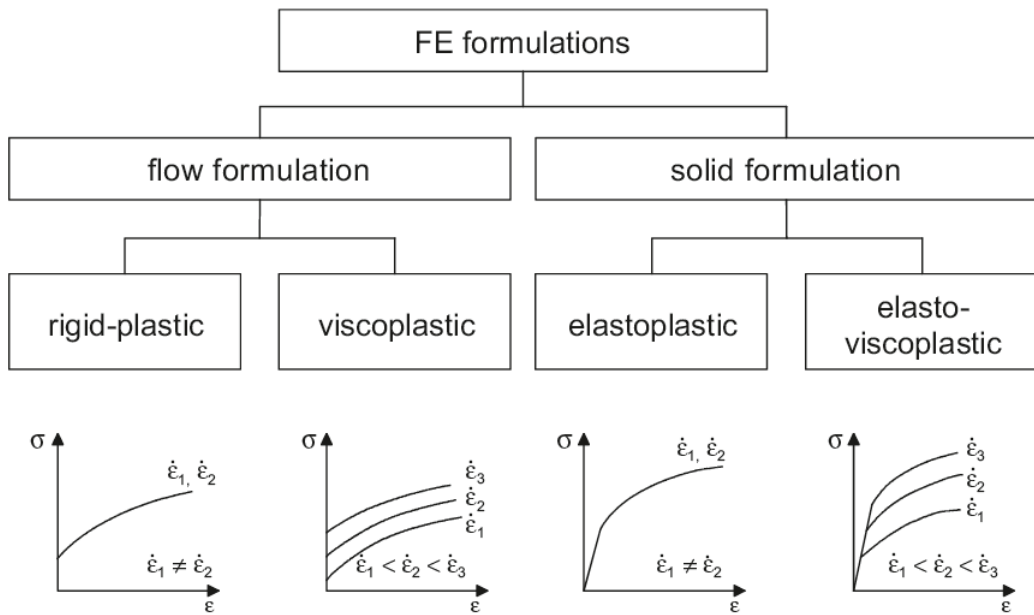


Figure 3.2: Finite element formulations Roll and Tekkaya [1993]

Depending on the objective of an FE analysis, two different approaches may be taken as illustrated in Figure 3.2. The first type of formulation considers the material rigid until plastic deformation begins. Usually, this formulation is referred to as “flow formulation” or “rigid-plastic formulation” (Kobayashi et al. [1989]; Wu et al. [2003].) The second type which

is referred to as “solid formulation” or “elastoplastic formulation” considers the material as elastic until the elastic limit is exceeded after which plastic deformation begins. The flow formulation is used to reduce computation time if the amount of plastic deformation outweighs the amount of elastic deformation significantly. However, if elastic effects such as springback and residual stresses are of interest, the solid formulation has to be used (Wu et al. [2003]; Roll and Tekkaya [1993]).

Strain rate dependence as captured in the viscoplastic or the elasto-viscoplastic formulation is important to take into account processes that are conducted at elevated temperatures or processes that involve high strain rates such as machining processes.

Within this thesis, an elasto-viscoplastic formulation is used to model the machining process.

3.8 Finite element modeling of machining

In this section, some aspects of the finite element method which are essential in building a realistic model of the metal cutting process are presented. This involves, among other topics, the presentation of the model formulation, the application of modeling strategies on mesh generation, the determination of boundary conditions and the modeling of workpiece material and tool-chip interface. Although this discussion involves techniques generally used in finite element analysis, the application to machining is documented here. Depending on the selection of the correct parameters, some important features such as cutting forces, temperatures and chip morphology are influenced and determined. For example in FEM cutting models, the workpiece material law and the friction model at the tool-chip interface are considered of great importance for the outcome of the analysis. Many simulations are concerned only with the determination of these two factors in order to provide as accurate as possible predictions, where accuracy here means results that show as little as possible discrepancies between model and experiment. The results may be used for the determination of tool wear and surface quality characteristics.

3.8.1 Meshing

The initial mesh of the workpiece is very significant for the results produced by the model. The convergence of the numerical procedure and the accuracy of the predicted variables depend on it. The mesh must be able to accurately represent the workpiece geometry and must also be composed of an element which is capable of handling the performed analysis. There are both structured and unstructured mesh generation algorithms implemented in commercial finite

element codes for the arrangement of elements in the continuum but how these algorithms are employed depends on the problem at hand. The size, number and type of elements used in the mesh play a significant role in the simulation outcome.

A larger number of small sized elements increases accuracy but also increases computational time. There is a threshold beyond which further increases in the number of elements will significantly increase the time of the analysis with marginal gain in accuracy. Usually, a coarser mesh is employed for testing a model due to savings in time and a finer mesh is used for the final simulation when all goes well. Another technique is to identify the regions that are of more interest to the analysis. Finer meshes may be used in such regions and coarser meshes used in the other parts of the model which are of less interest. In machining, most of the action occurs in the primary and secondary deformation zones. Therefore the mesh at this part of the model is expected to be denser in order to obtain better chip geometry and also cope with the expected strains, strain rates and temperature gradients.

An element with a compact and regular shape is expected to perform better and loses its accuracy as the aspect ratio of the element increases. Low order elements often equipped with formulations to avoid volumetric locking behavior that can halt the analysis due to large plastic strains in metal cutting, are widely used due to their simplicity.

3.8.2 Contact

Machining involves contact between deformable bodies, i.e. workpiece and tool. Mesh-on-mesh contact can also occur between detached segments of the workpiece in the form of chip and the workpiece itself. The most common algorithms used for solving contact problems are the penalty approach, the Lagrangian multiplier method and the augmented Lagrangian method. Other procedures such as the perturbed Lagrangian method are also reported in the literature. For a comprehensive literature review on some of these contact methods, see Vaz et al. [2007].

In the penalty formulation, normal forces are obtained by insertion of contact stiffness when a material point on the contact body (master) penetrates a target body (slave). However, the impenetrability condition is not exactly fulfilled in the penalty approach since the contact stiffness will have to be excessively high. High contact stiffness however leads to a poorly conditioned system stiffness matrix, which in turn may lead to numerical problems. Therefore accuracy and convergence efficiency have to be balanced. The advantage of this procedure is that only displacements are solved.

In contrast to the penalty formulation, the Lagrangian multiplier algorithm ensures exact satisfaction of the required contact constraints (Crisfield [1997]). The multipliers can be

interpreted as contact forces. However, the disadvantage of this method is the searching that has to be undertaken for displacements and forces which leads to an increase in computational time.

It is possible to combine the penalty method and the Lagrangian multiplier method into what is called the augmented Lagrangian method, with the aim of retaining the good merits of each approach. The main advantage of this method is that rather than increasing contact stiffness in order to achieve exact adherence to the required contact constraints, as done in the case of the penalty method, contact forces are augmented. As a result, the problem of a poorly conditioned system matrix is avoided.

In this thesis, the penalty method is used due to the fact that it is readily available in the choice of FEM simulation package used in this work.

3.8.3 Material modeling

Material modeling in machining is of great importance especially the flow properties of the workpiece material and the corresponding equations that are used to describe the behavior of the material in the FEM simulation. These equations describe the flow stress or instantaneous yield strength at which the workpiece material starts to plastically deform or flow. In metal cutting, the elastic strains are much lower than the plastic strains therefore the workpiece material flows plastically in the primary cutting zone.

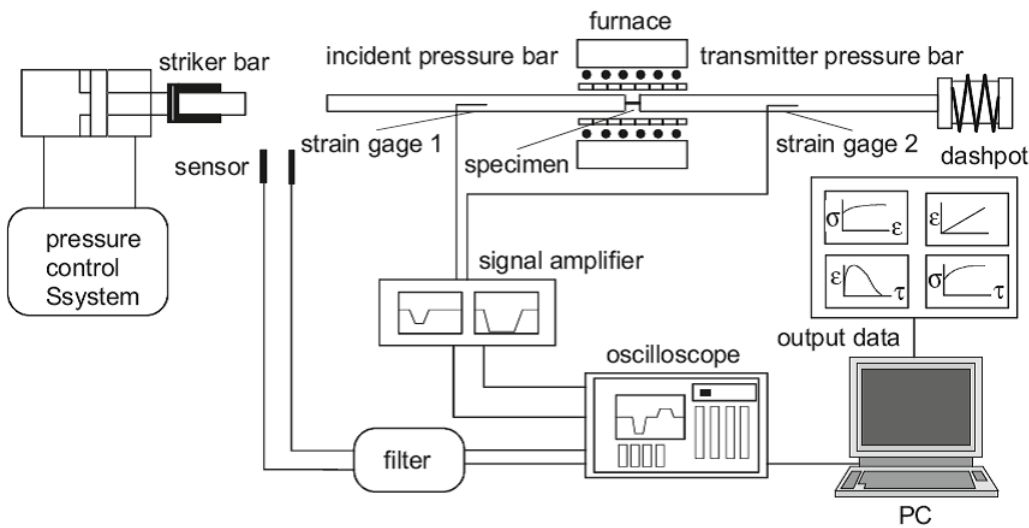


Figure 3.3: Split Hopkinson Pressure Bar setup (Lee and Lin [1998]).

Machining of ductile metals can be considered as a localized forming process, or respectively, a wedge indentation that takes place at high strain rates and temperatures (Tönshoff [1995];

Madhavan et al. [1998]). The workpiece material deforms plastically and experiences strain rates within a magnitude of 10^4 s^{-1} during standard machining and 10^6 s^{-1} in high speed machining in the shear zone (Hoppe [2003]; Bäker [2004]). In addition, temperatures of up to 1200°C are reported in the shear zone (Jaspers and Dautzenberg [2002]). In contrast to most forming operations, strongly localized plastic deformations occur in metal cutting. The locally occurring strains and strain rates exceed the conditions that can experimentally be reproduced in a manner that allows the acquisition of strains, stresses and temperatures in order to provide experimental flow stress data for use in machining models. There are mainly two different approaches used in the acquisition of these data. The first approach is the conduction of a high speed compression test, such as the Split-Hopkinson-Pressure-Bar (SHPB) test and the extrapolation acquisition of the required data which is described by means of a constitutive model and implemented in the FEM simulation of the cutting process (Lee and Lin [1998]). A typical test set up is shown in Figure 3.3, the specimen is held between two straight bars, the incident bar and the transmitter bar, and a furnace allows heating of the specimen to desired temperature. A third bar known as the striker bar is pneumatically accelerated and its velocity is measured by sensors. The striker bar hits the incident bar and induces a mechanical wave which propagates through the bar. The wave reaches the specimen and causes it to deform or fracture while part of the wave is reflected back into the incident bar. The specimen response modifies the incident wave and the modified wave propagates through the transmitter bar. Based on the one dimensional elastic wave propagation theory, the recorded pulses ε_i , ε_r and ε_t can be utilized to determine the average strain ε , strain rate $\dot{\varepsilon}$ and stress σ within the specimen, assuming a uniform deformation, by making use of the following expressions

$$\begin{aligned}\varepsilon &= \frac{2C_0}{L_0} \int \varepsilon_t dt, \\ \dot{\varepsilon} &= \frac{2C_0 \varepsilon_r}{L_0}, \\ \sigma &= E \frac{A}{A_0} \varepsilon_t,\end{aligned}\tag{3.2}$$

where ε_i is the incident pulse, ε_r reflected pulse, and ε_t transmitted pulse. Furthermore C_0 is the longitudinal wave velocity, L_0 is the length of the specimen, E is the Young's modulus, A is the cross sectional area of the split bar and A_0 is the cross sectional area of the specimen.

The second approach for an experimental determination of flow stress data for machining simulations is an inverse analysis technique based on actual machining experiments as e.g. suggested by Shatla et al. [2001a,b]. Rather than using the results of compression tests and extrapolating them by means of an empirical equation (constitutive equation), this method

assumes an analytical model, such as presented in the work of Oxley [1989], which is able to predict process forces and temperatures. The experimentally acquired forces serve as a benchmark for the analytical model which tunes the parameters of a flow stress equation assumed to follow a constitutive model until the predicted cutting forces match the experimental results with a specified error tolerance. In Shatla et al. [2001a,b], the material specific flow stress parameters are determined iteratively by minimizing the error between the predicted and experimentally determined forces. This minimization objective is formulated as a multi-dimensional minimization problem which is solved by means of algorithms such as the Downhill-Simplex algorithm. Although this approach has a lot of inherent advantages, it also has some disadvantages. Assumptions made in the analytical model potentially reduce the accuracy of the obtained flow stress curve. Furthermore, the analytical model can only predict flow stress curves for materials which are machined by sharp tools and form continuous chips.

A third approach which is based on the minimization of the error between finite element simulations of the cutting process and actual cutting experiments has been proposed by Klocke et al. [2013]. In this approach, some of the material specific flow stress parameters are identified through a quasi-static compression experiment whereas the rest are identified through a full factorial simulation schedule of the cutting test. The simulation results are systematically compared to experimentally obtained process outputs such as chip morphology, workpiece temperature and cutting forces. The parameters which result in the correct prediction of the experimental process outputs are identified by interpolation. Compared to inverse identification by means of an analytical model, the present approach yields better material parameters due to the ability of the finite element model to predict more complex process outputs (e.g. chip morphology and stress distribution).

The advantage of the inverse method over the SHPB method is the fact that it is less expensive. Additionally, the maximum strain rate which is possible with the SHPB method is around 10^4 s^{-1} whereas actual strain rates experienced in high speed machining is around 10^6 s^{-1} with temperatures in the deformation zones close to the melting point of the workpiece material ($T/T_{melt} = 0.9$), see Jaspers and Dautzenberg [2002]. This means an extrapolation of the SHPB results is required which could result in inaccuracies in the obtained flow stress data. However, this is not the case for the inverse method since the flow stress data is identified from actual orthogonal cutting tests.

In this work the flow stress data obtained by Klocke et al. [2013] for Inconel 718 by means of inverse identification is employed.

Although there are many constitutive models available in the literature for describing the behavior of metals at high strains, strain rates and temperatures, a few of them are discussed

in the following paragraphs. The first of these models proposed by Usui et al. [1981] and Shirakashi et al. [1983] is expressed as

$$\sigma = B \left(\frac{\dot{\varepsilon}}{1000} \right)^M e^{-kT} \left(\frac{\dot{\varepsilon}}{1000} \right)^m \left(\int_{\text{path}} e^{KT/N} \left(\frac{\dot{\varepsilon}}{1000} \right)^{-m/N} d\varepsilon \right)^N, \quad (3.3)$$

where B is the strength factor, M the strain rate sensitivity and N the strain hardening index. Furthermore, T is the workpiece temperature whereas k and m are material constants. The integral term accounts for the history effects of strain and temperature in relation to strain rate. In the absence of these effects, (3.3) is reduced to (Childs et al. [1994])

$$\sigma = B \left(\frac{\dot{\varepsilon}}{1000} \right)^M \varepsilon^N. \quad (3.4)$$

One of the most widely used material models in cutting simulation is the model proposed by Johnson and Cook [1983]. The equation is a thermo-elasto-viscoplastic material constitutive model which consists of three terms. The first term models strain hardening effects, the second term accounts for strain rate dependence and the third term models temperature softening effects. It is expressed as

$$\sigma = (A + B\varepsilon^n) \left(1 + C \ln \left(\frac{\dot{\varepsilon}}{\dot{\varepsilon}_0} \right) \right) \left(1 - \left(\frac{T - T_0}{T_m - T_0} \right)^m \right), \quad (3.5)$$

where ε is the equivalent plastic strain, $\dot{\varepsilon}_0$ is the reference equivalent plastic strain rate, T is the workpiece temperature, T_0 is the ambient temperature and T_m is the melting temperature. The coefficient A is the yield strength, B is the hardening modulus, C is the strain rate sensitivity coefficient, n is the hardening coefficient and m is the thermal softening coefficient. The material parameters are constants that depend on the material and are obtained by fitting the equation to flow stress data obtained from an SHPB test (Lee and Lin [1998]) or by inverse identification method (Klocke et al. [2013]; Shatla et al. [2001a,b]).

Zerilli and Armstrong [1987] also developed a constitutive model based on dislocation mechanics, where the crystal structure of the workpiece material is taken into account. For a body centered cubic (BCC) lattice structure, the constitutive equation is expressed as

$$\sigma = C_0 + C_1 \exp(-C_3 T + C_4 T \ln \dot{\varepsilon}) + C_5 \varepsilon^n \quad (3.6)$$

whereas for a face centered cubic (FCC) lattice structure, the constitutive equation is expressed

as

$$\sigma = C_0 + C_2 \varepsilon^n \exp(-C_3 T + C_4 T \ln \dot{\varepsilon}). \quad (3.7)$$

The coefficients C_i ($i = 0 \dots 5$) and n are material parameters which are determined experimentally by means of a SHPB test, see e.g. Meyer and Kleponis [2001].

In this thesis, the Johnson and Cook constitutive model is used.

3.8.4 Friction modeling

Friction modeling in the secondary deformation zone, at the interface of the chip and the rake face of the tool is of equal importance as the workpiece material modeling presented in the previous paragraphs. It is important in order to determine the cutting force but also tool wear and surface quality. Many finite element models of machining assume the shear stress (traction) τ_f acting on the tool rake face is either a case of classical friction, i.e. Coulomb's law, where the frictional sliding force is proportional to the applied normal stress σ_n

$$\tau_f = \mu \sigma_n, \quad (3.8)$$

with the coefficient of friction μ as the constant of proportionality, or a case of shear friction law where the frictional sliding force is proportional to $k_f/\sqrt{3}$

$$\tau_f = m \frac{k_f}{\sqrt{3}}, \quad (3.9)$$

where m is the constant of proportionality or constant shear factor and k_f is the local flow stress of the workpiece material. However, the Coulomb friction law fails to give accurate predictions as the normal stress increases and surpasses a critical value.

From experimental analysis it has been verified that two contact regions may be distinguished in dry machining, namely sticking and sliding region. Zorev [1963] suggested a stress distribution in the chip contact zone on the tool rake face as shown in Figure 3.5. The normal stress shows a maximum at the cutting edge and then decreases exponentially until it reaches zero at the end of the contact zone (A-C). The rake face is divided into a sticking and a sliding region. In the sticking region (A-B) the frictional shear stress (traction) is assumed to be equal to the local shear flow stress of the workpiece material which results in

$$\tau_f = \frac{k_f}{\sqrt{3}} \quad (3.10)$$

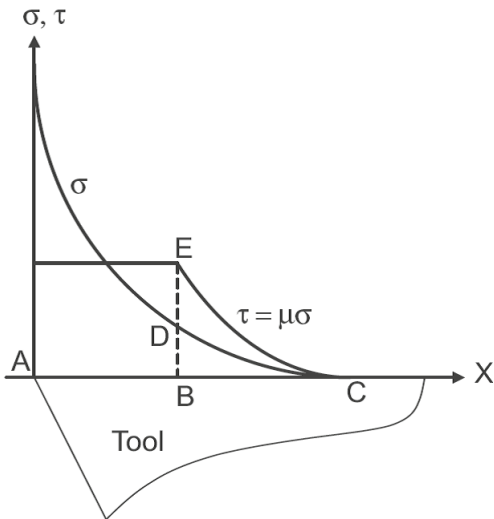


Figure 3.4: Normal and frictional stress distribution along the rake face as suggested by Zorev [1963]

Based on Zorev [1963] and experimental results, Usui et al. [1981] proposed a nonlinear shear stress normal stress relation which is expressed as

$$\tau_f = \frac{k_f}{\sqrt{3}} \left(1 - \exp \left(-\frac{\mu\sigma_n}{k} \right) \right). \quad (3.11)$$

As the normal stress $\sigma_n \rightarrow \infty$ in 3.11, the sticking part of the model proposed by Zorev [1963] is reached whereas the sliding part is reached as $\sigma_n \rightarrow 0$.

Childs and Maekawa [1990] also modified the model proposed by Usui et al. [1981] as follows

$$\tau_f = m \frac{k_f}{\sqrt{3}} \left(1 - \exp \left(-\frac{\mu\sigma_n}{k} \right) \right)^{1/n}, \quad (3.12)$$

where m and n are correction factors. The former ensures that at high normal stresses, the frictional stresses do not exceed k and the latter controls the transition from sticking to sliding region. These coefficients can be obtained by the split-tool method.

Although there has been a great amount of work done on friction in metal cutting, uncertainty in the description of the friction conditions between tool and workpiece still remains. This uncertainty is due to the lack of experimental methods that allow the verification of the friction models. To experimentally verify the friction models, one has to determine the normal and shear stress distribution along the tool rake face. An approach to experimentally obtain stress distribution along the tool rake face in machining processes is the split tool method as described in Gordon [1967].

Despite the availability of advanced friction models for machining, most researchers have

chosen to rely on a Coulomb law or the shear friction law. Two significant reasons for this approach are the dependency of the advanced laws on constants which are difficult to determine as well as the negative numerical impact of these friction models which may result in convergence issues. A Coulomb friction model is used in this thesis work.

3.8.5 Modeling material separation

An important aspect of metal cutting simulation based on a Lagrangian formulation is the correct modeling of the material separation in front of the tool. Possible approaches are either to predefine a separation line and then separate the nodes on this line when a certain criterion is reached (this criterion is purely a geometrical criterion) or to use a more flexible approach where the separation line is determined by a physical criterion, which can either be a critical stress criterion or a damage model to determine the separation. A third approach is also possible where no true material separation is done and the machining process is considered as a pure deformation process similar to forging (Bäker et al. [2002]).

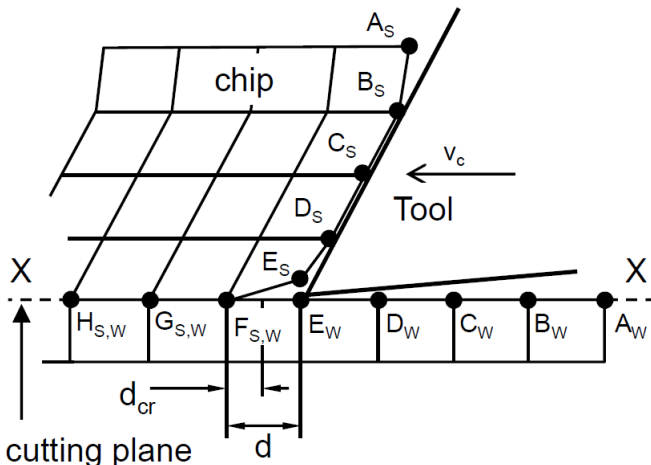


Figure 3.5: An illustration of a geometrical node separation (Klocke [n.d.]).

According to the geometrical criterion, node separation is started when the tool tip approaches a node along a predefined parting line within a critical distance. This process can be seen in detail in Figure 3.5, assuming the critical distance between the tool tip and the nearest node on the cutting direction is d_{cr} . When the distance d between the tool tip and the node E becomes equal or less than the critical distance, node separation occurs. In Figure 3.5, node separation has already occurred. The node E is split into two nodes E_S and E_W . The node E_S moves in the direction of the chip becoming part of the chip whilst the node E_W stays on the machined surface remaining as part of the workpiece. This criterion is only

based on geometrical considerations and the critical distance is chosen arbitrarily. Hence it cannot account for breakage outside the cutting line and therefore lacks the ability to display the physical mechanism behind chip formation. In Bäker et al. [2002] it is explained that this method can lead to convergence problems due to movement of nodes in wrong directions. For instance instead of node E_W moving in the direction of the machined surface it moves in the direction of the chip or node E_S moves in the direction of the machined surface or both move in opposite directions. To prevent such occurrences, two auxiliary contact surfaces are introduced; one acts on the nodes of the workpiece and the other acts on the nodes of the chip. It is further reported that these auxiliary surfaces have an effect on cutting forces. Furthermore, different critical distances result in different plastic strain distribution (Lin and Lin [1992]). On the other hand, the geometrical separation method is easy to control and can be used for cutting tools without sharp edges. This technique has been used by many authors, see e.g. Huang and Black [1996]; Obikawa and Usui [1996].

Material separation based on physical criteria uses the critical value of a physical quantity to estimate the onset of material separation. There are a lot of damage models based on some of these physical criteria such as strain, stress, energy density etc. to either accomplish nodal separation, element deletion or material flow stress reduction in the finite element mesh which leads to a representation of chip formation. For example, Marusich and Ortiz [1995] introduced a fracture criterion based on the critical stress for brittle mode fracture and another based on effective plastic strain for ductile failure, to achieve chip breakage. Obikawa et al. [1997] also used a criterion based on equivalent plastic strain to produce discontinuous chips by causing crack nucleation and growth when the equivalent plastic strain exceeds the fracture strain. In the following paragraphs, two of these damage models are reviewed.

The first model is the damage model proposed by Cockcroft and Latham [1968] which is based on the consumed mechanical energy and is expressed as

$$D_{\text{crit}} = \int_{\varepsilon} \max(\sigma_1, 0) d\varepsilon. \quad (3.13)$$

It says that when the integral of the maximum principal stress σ_1 over the plastic strain path reaches a critical damage value D_{crit} , material fracture should occur. The critical damage value D_{crit} can be determined by experimental test or by the method of inverse identification as done in Klocke et al. [2013]; Umbrello [2008]. To display the occurring fracture in the simulation model, two methods are employed. In the first method, the material flow stress at the point where D_{crit} is reached is lowered to a value p which is a percentage of the original flow stress. As a result of the decrease in flow stress, the characteristic serrated chip geometry in Figure

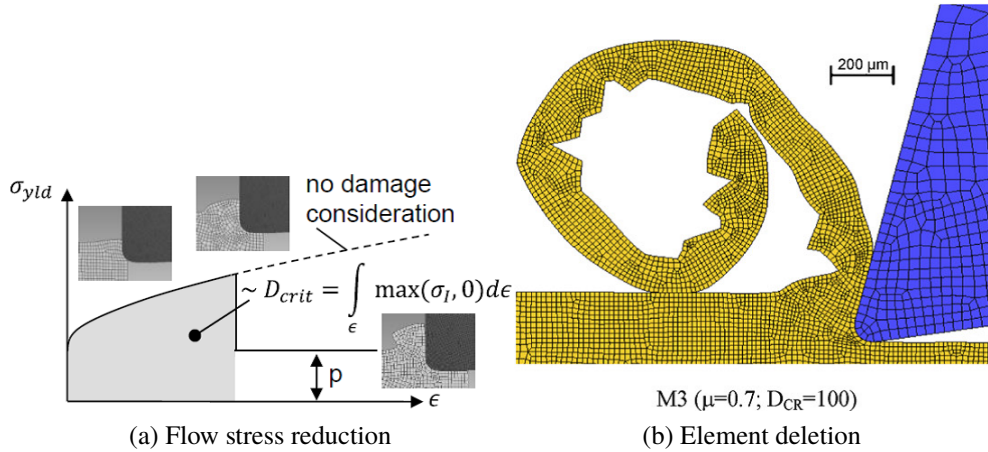


Figure 3.6: Cockcroft and Letham damage criterion for the prediction of serrated chip formation; (a) flow stress reduction Klocke et al. [2013]; (b) element deletion and element rough edge smoothing Umbrello [2008].

3.6a is observed. This type of serrated or saw tooth chip geometry is mostly observed in high speed cutting of superalloys. Another approach is to delete the elements within which D_{crit} is reached and to smooth the rough boundaries of the resulting elements as done in Umbrello [2008], see Figure 3.6b.

Johnson and Cook [1985] also proposed a damage model which is based on an equivalent plastic strain criterion. The damage parameter ω is defined as

$$\omega = \sum \left(\frac{\Delta \varepsilon}{\varepsilon_f} \right), \quad (3.14)$$

where ε_f is the equivalent plastic strain to fracture or failure strain and $\Delta \varepsilon$ is the increment of equivalent plastic strain. The expression of failure strain is given as

$$\varepsilon_f = \left(d_1 + d_2 \exp \left(-d_3 \frac{\sigma_m}{\sigma_{vM}} \right) \right) \left(1 + d_4 \ln \left(\frac{\dot{\varepsilon}}{\dot{\varepsilon}_0} \right) \right) \left(1 + d_5 \left(\frac{T - T_0}{T_m - T_0} \right) \right), \quad (3.15)$$

where d_i ($i = 1 \dots 5$) are material constants which are material specific and are determined from experiments such as tensile Split Hopkinson bar test or ballistic test. Alternatively, an inverse identification method can be employed. For the case of experimental determination of the parameters d_i ($i = 1 \dots 5$), careful adjustments of the parameters has to be carried out until a suitable fit to experimental data is obtained, see Gregory [2003]. The failure strain as seen in (3.15) is a function of a dimensionless plastic strain rate $\dot{\varepsilon}/\dot{\varepsilon}_0$ ($\dot{\varepsilon}_0$ is the reference strain rate), stress triaxility σ_m/σ_{vM} (σ_m is the hydrostatic stress and σ_{vM} is the equivalent stress)

and a dimensionless temperature. In this model, failure is reached when the damage parameter $\omega > 1$ by which case the accumulated equivalent plastic strain would have been equal to the failure strain. In the commercial finite element solver ABAQUS/explicit, when the failure criterion is met, the deviatoric stress components in the element are set to zero and remain zero for the rest of the analysis. Depending on the choice of the user, the pressure may also be set to zero in which case element deletion may be specified or the element may be required to remain compressive for the rest of the analysis. For the simulation of chip formation, it is required that the elements be deleted.

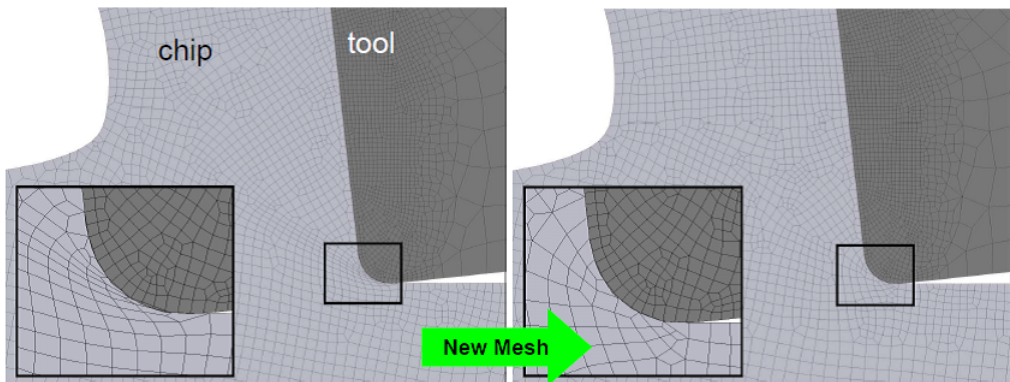


Figure 3.7: Material separation as a result of remeshing Klocke [n.d.].

A third approach for modeling material separation is by a pure deformation procedure. In this method, the metal cutting process is simulated without real node separation or element deletion. Instead, it can be considered as a deformation process (Sekhon and Chenot [1993]). As the tool advances, elements tend to deform strongly as shown in Figure 3.7. The distorted elements are refined during a remeshing step. Frequent remeshing is necessary to ensure elements are not strongly distorted. The case shown uses a tool with a rounded edge which leads to a reduction in workpiece material penetration. The situation is worse for a tool with an infinitesimally sharp edge as material penetration will be higher and may require frequent remeshing. This simple approach has the advantage of easy convergence, as no discontinuity occurs as compared to the geometrical nodal separation procedure. Additionally no auxiliary contact surfaces have to be specified since nodes which move in the direction of chip instead of workpiece material can be corrected after a remeshing process. The disadvantage of this method is the fact that it is susceptible nonphysical loads between tool and workpiece since the distorted elements are only refined in a remeshing process.

In this thesis, material separation is accomplished by the Johnson-Cook damage model. The reason for choosing the aforementioned model is because it is readily available in ABAQUS/explicit. Additionally, it is based on a physical separation criterion which means

predicted chips are likely to follow experimental trend.

3.8.6 Adaptive meshing

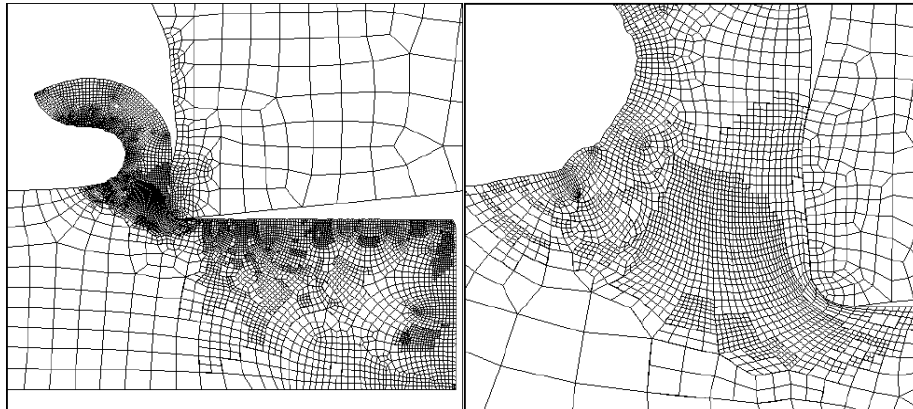


Figure 3.8: Refined finite element mesh based on a combination of plastic work rate and displacement gradient Kalhor [2001].

In the Lagrangian formulation, the initial mesh is altered significantly due to plastic deformation and chip separation. The distorted mesh causes numerical errors and the solution is rapidly degraded. Furthermore, the Jacobian determinant becomes negative for severe distortion and the analysis is halted. Additionally, high mesh densities are required for the simulation of the cutting process. To obtain accurate results and to simultaneously decrease computational time, adaptive remeshing schemes become an invaluable tool.

An adaptive mesh refinement involves the improvement of an existing mesh based on error estimates for that mesh. Mesh adaptivity is divided into three different categories, H-adaptivity, P-adaptivity and R-adaptivity. H-adaptivity consists of changing the size of the element which may either lead to a local refinement of the mesh or coarsening of the mesh, P-adaptivity refines the polynomial order of the element shape functions and R-adaptivity consists of relocation of element nodes without changing the mesh connectivity.

Mesh adaptivity, for an efficient meshing, requires two essential ingredients, a tool for assessing the error of the solution computed for a given mesh and an algorithm to define a new spatial discretization (Kalhor [2001]). In the literature, some researchers such as Zienkiewicz and Zhu [1992, 1987]; Hyun and Lindgren [2001]; Runnemalm and Hyun [2000] proposed an error estimator for linear elements based on the discontinuity of the gradient of displacement of elements at inter-element boundaries or heat flux. This means, a mesh will be refined where large differences in gradients exist between elements. Marusich and Ortiz [1995] proposed the

use of the plastic work rate in each element for mesh refinement in cutting simulations. The aim of this method is to capture the plastic deformation of the workpiece material. Owen and Jr. [1999] also proposed an error estimator based on the rate of fracture indicators which aims to not only capture the progression of the plastic deformation but to also provide a fine mesh at regions of possible material failure.

For defining a new spatial discretisation, the Delauney triangulation method for the generation of six-noded quadratic elements was employed in Marusich and Ortiz [1995]. This was accomplished by adding more nodes to elements which fulfilled the plastic work rate criterion. In most cases, multiple mesh adaptivity schemes have to be combined in order to maintain a good mesh quality. In Kalhor [2001] for instance, H- and R-adaptivity are combined to simulate the cutting process.

Even though adaptive meshing is necessary for reducing excessive element distortion which means improvement of the accuracy of the simulation, it has a computational cost. This is attributed to the newer mesh being denser and thus more elements are involved in the analysis, but also to error and distortion metrics, for the assessment of mesh quality of the solution and transfer operators which are responsible for transferring the variables of the old mesh to the new mesh. Figure 3.8 shows an example of an adaptive meshing technique as it pertains to cutting simulation.

In this thesis, a remeshing scheme is not employed. This is due to the unavailability of such schemes for fully coupled thermal stress analysis in ABAQUS/explicit.

3.8.7 Finite element software packages

In earlier times, researchers wrote their own finite element codes for specific processes such as metal cutting analysis. For the past 20 years a wide range of commercial FEM packages have become available. These programs have been widely accepted by researchers since they can simplify the overall procedure of model building. Commercial FEM adds to the quality and accuracy of the produced models. These programs are made by specialist who have tested them and have implemented features and procedures to accelerate the slow procedure of model building. Most of the software products have mesh generation programs, easy to use menus for applying boundary conditions, contact algorithms, automatic remeshing, material databases etc. Even though the complexities of model building are reduced by these FEM software products, they tend to impose a lot of limitations on the models that can be built e.g. a model may only be able to solve a problem implicitly or explicitly.

Regarding machining, some of the FEM codes that have been used for the simulation of machining include: ABAQUS, FORGE 2, DEFORM 2D/3D, LS-DYNA, AdvantEdge etc.

While some of these programs are general purpose finite element software others are specific purpose finite element software. ABAQUS for instance is a general purpose finite element program which allows a user to model systems with a high level of detail. With regards to modeling machining it proves to be particularly challenging since it does not have remeshing capabilities. LS-DYNA is a program used mainly in crashworthiness analysis and forming problems, DEFORM 2D is a program for forming processes, which has a machining module to accommodate turning, milling, boring and drilling operations. AdvantEdge is a Lagrangian, explicit, dynamic code which is only used for simulating machining.

It is argued and backed-up with experiments that the discrepancies between modeling and experimental results lay with the material and the conditions not with the failure of the software to simulate machining. It is agreed that cutting and feed forces are not correctly predicted at the same time, the latter being underestimated. This can be corrected by altering the friction parameters or as suggested by Childs and Rahmad [2009a]; Childs [2009]; Childs and Rahmad [2009b] by incorporating the effect of yield delay in the material model, a phenomenon which occurs when machining carbon steels at elevated speeds.

4 | Orthogonal cutting experiment and simulation

4.1 Orthogonal cutting experiment

In this section, the experimental setup is described. Furthermore, the obtained experimental results, such as forces, temperatures, chip thicknesses and chip morphology, are discussed.

4.1.1 Experimental setup

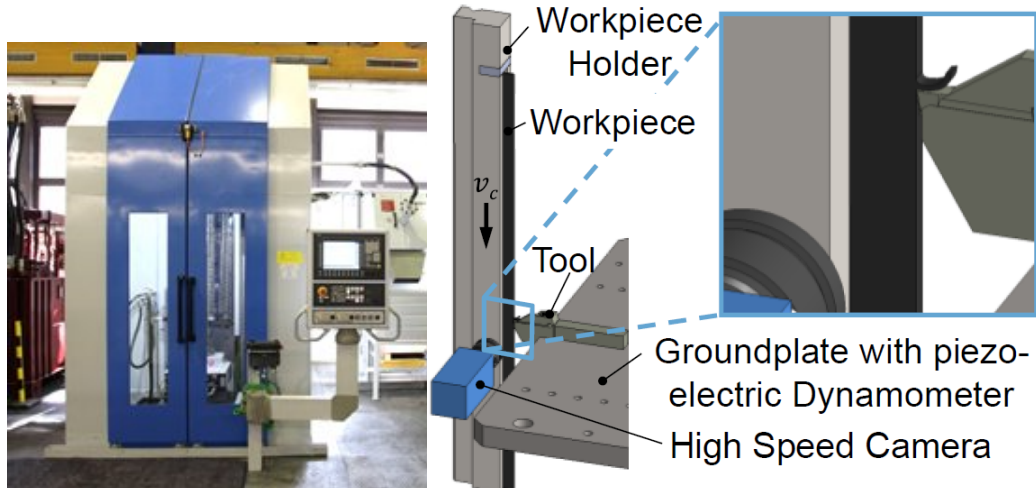


Figure 4.1: Setup for orthogonal cutting test (courtesy WZL).

To check the accuracy of the simulated orthogonal cutting results, the results are compared to experimental cutting forces, chip geometries and machined surface temperature. To facilitate this, orthogonal cutting tests were performed at the Werkzeugmaschinenlabor (WZL) at RWTH Aachen University. Depicted in Figure 4.1 is the setup for the orthogonal cutting test. The machine used for the broaching operation is a Forst RASX 8x2200x600M/CNC. It has a workpiece holder which moves while the cutting tool is held in place by a groundplate with a

piezoelectric dynamometer for the measurement of the forces acting on the tool. In addition, there is also a high speed camera for the filming of the chip formation process. In contrast to the conventional orthogonal machining setups (face turning by a lathe machine) used in most cutting tests for the acquisition of experimental data, this broaching machine allows a direct comparison between experimentally acquired data and two dimensional orthogonal cutting simulation of the cutting process due to the linear geometry of the workpiece. The workpiece used in the experimental cutting test is aged nickel-based superalloy Inconel 718 with a length of 100 mm, a breath of 50 mm and a thickness of 3.5 mm.

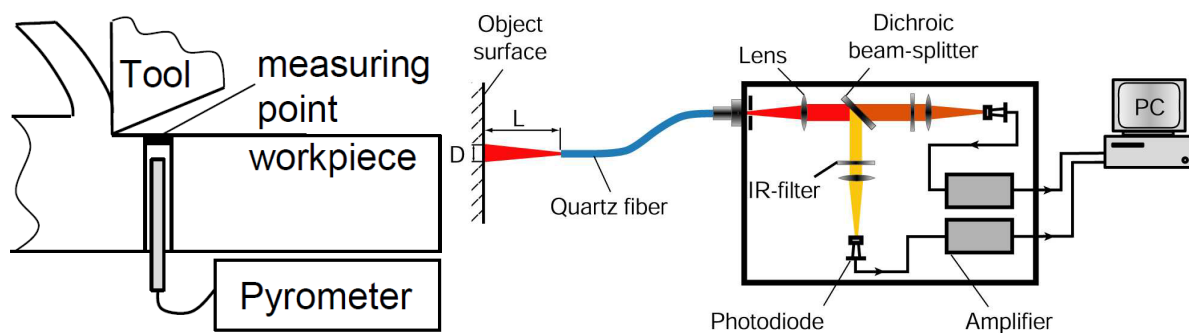


Figure 4.2: Setup for the determination of the machined surface temperature (courtesy WZL).

Cutting temperatures of the workpiece were measured by means of a two color pyrometer. The optical fiber that forwards the wave spectrum from the measuring spot to the analyzer was mounted through a hole drilled at the base of the workpiece. Infrared spectrum via the optical cable is transmitted to the analyzer for signal analyses and amplification and then fed to a computer to display the measured temperatures as shown in the setup in Figure 4.2.

The cutting inserts used in the experiment were uncoated carbide grade inserts (H13A). They combine good abrasive wear resistance and toughness. All tool rake angles were 0° , all tool flank angles were 10° and the cutting edge radii were $r_\beta = 10 \mu\text{m}$, $20 \mu\text{m}$ and $30 \mu\text{m}$. The tool rake faces were flat, no chip formers were used. Furthermore the cutting velocities were $V_c = 20 \text{ m/min}$, 40 m/min and 80 m/min and the feed was $f = 0.05 \text{ mm}$.

The experimental plan for the conducted cutting tests consisted of nine sets of cutting operations performed under different cutting conditions as shown in Table 4.1. The cutting conditions are chosen to cover a wide range of process conditions. In order to provide statistically valid data, the cutting tests corresponding to each parameter set were repeated three times. All experiments were conducted without the use of a coolant in order to simplify the finite element simulation.

Table 4.1: Experimental plan for cutting test

Parameter set	r_β [μm]	f [mm]	V_c [m/min]
1, 2, 3	10	0.05	20, 40, 80
4, 5, 6	20	0.05	20, 40, 80
7, 8, 9	30	0.05	20, 40, 80

Table 4.2: Experimentally obtained cutting and feed forces at all three combinations of cutting speed and cutting edge radii

r_β [μm]	$V_c = 20$ m/min		$V_c = 40$ m/min		$V_c = 80$ m/min	
	F_c^{exp} [N]	F_f^{exp} [N]	F_c^{exp} [N]	F_f^{exp} [N]	F_c^{exp} [N]	F_f^{exp} [N]
10	269	235	234	192	232	181
20	264	260	233	222	243	230
30	255	269	245	254	246	252

4.1.2 Forces and temperatures

The cutting forces F_c^{exp} and feed forces F_f^{exp} for the nine separate cutting conditions are recorded in Table 4.2 (note that F_f^{exp} is the same as F_t in Chapter 2). In order to compare 3D experiment to 2D simulation, the force obtained from the experiment has to be divided by the thickness of the workpiece to obtain specific forces.

Inferring from the results in Table 4.2 and the plots in Figure 4.4, it is observed that increasing cutting edge radius causes an increase in feed forces whereas an increase in cutting speed causes a decrease in feed forces. However, the cutting forces do not follow any particular trend, see Figure 4.3. This is because for lower cutting speeds e.g. $V_c = 20$ m/min, an increase in tool edge radius causes a correspondent decrease in cutting forces whereas the opposite tends to occur for $V_c = 80$ m/min.

Temperature measurements are performed in close proximity to the machined surface as shown in Figure 4.2. The measuring probe is placed at a distance of 4.5 mm behind the cutting tool. Displayed in Table 4.3 are the values for the maximum temperatures recorded for all three cutting speeds with a tool edge radius of $r_\beta = 10 \mu\text{m}$. Each value is an average of

Table 4.3: Measured temperature close to the machined surface for three different cutting speeds with a tool edge radius of $r_\beta = 10 \mu\text{m}$.

V_c [m/min]	T [$^\circ\text{C}$]
20	64.78
40	67.06
80	71.95

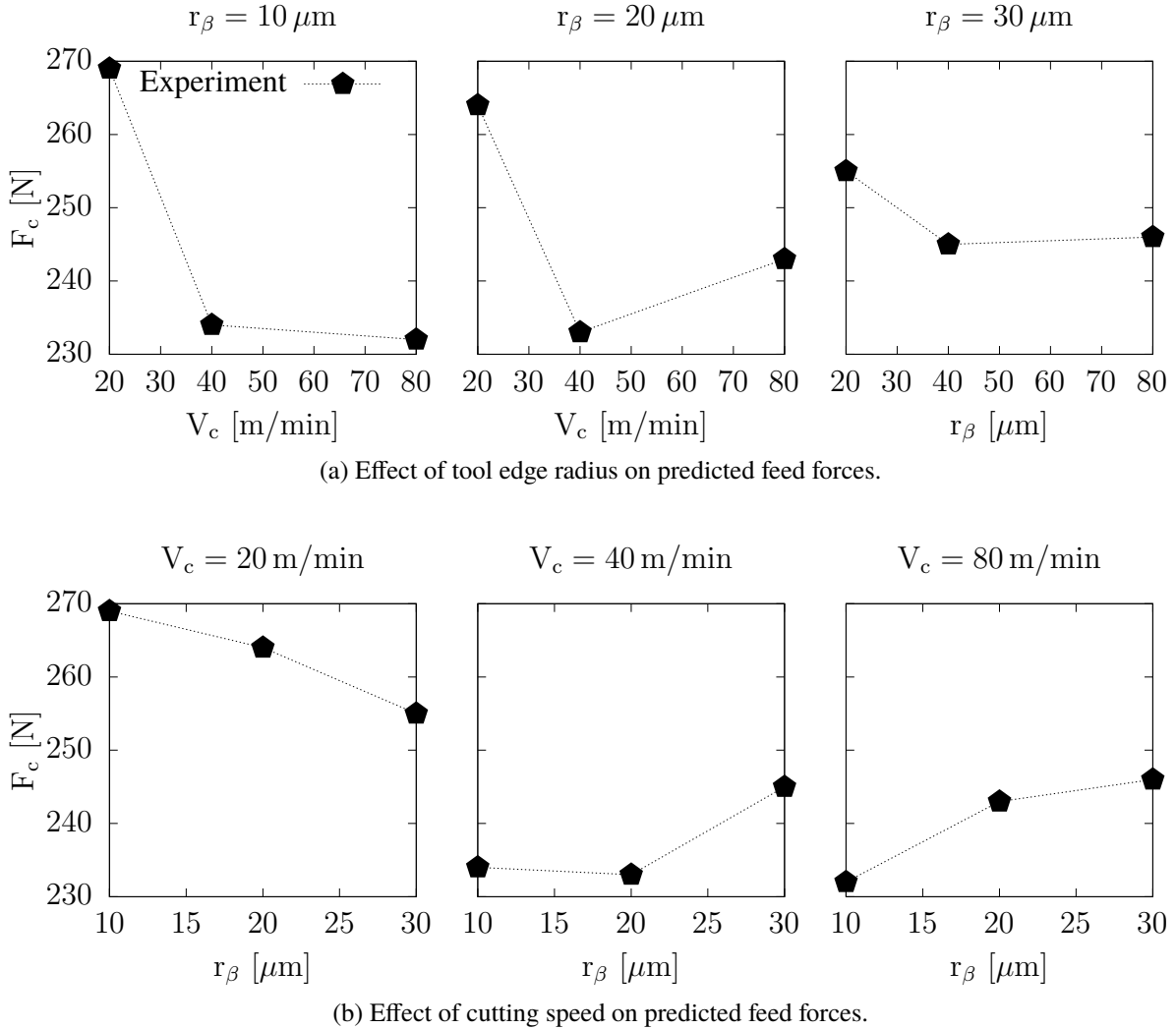


Figure 4.3: Effect of tool edge radius and cutting speed on feed forces.

three measurements. The recorded temperatures show an increase with cutting speed. This may be due to an increase in heat energy as a result of an increase in plastic deformation. Furthermore, a plot of temperature variation in the workpiece up to a depth of $500 \mu\text{m}$ for a cutting speed of $V_c = 40 \text{ m/min}$ is shown in Figure 4.5. From the plot, one can easily conclude that temperature rise in Inconel 718 is a highly localized process with the highest temperature change occurring in a depth of $100 \mu\text{m}$ below the machined surface, beyond which the temperature of the workpiece is generally at room temperature ($T = 25^\circ\text{C}$).

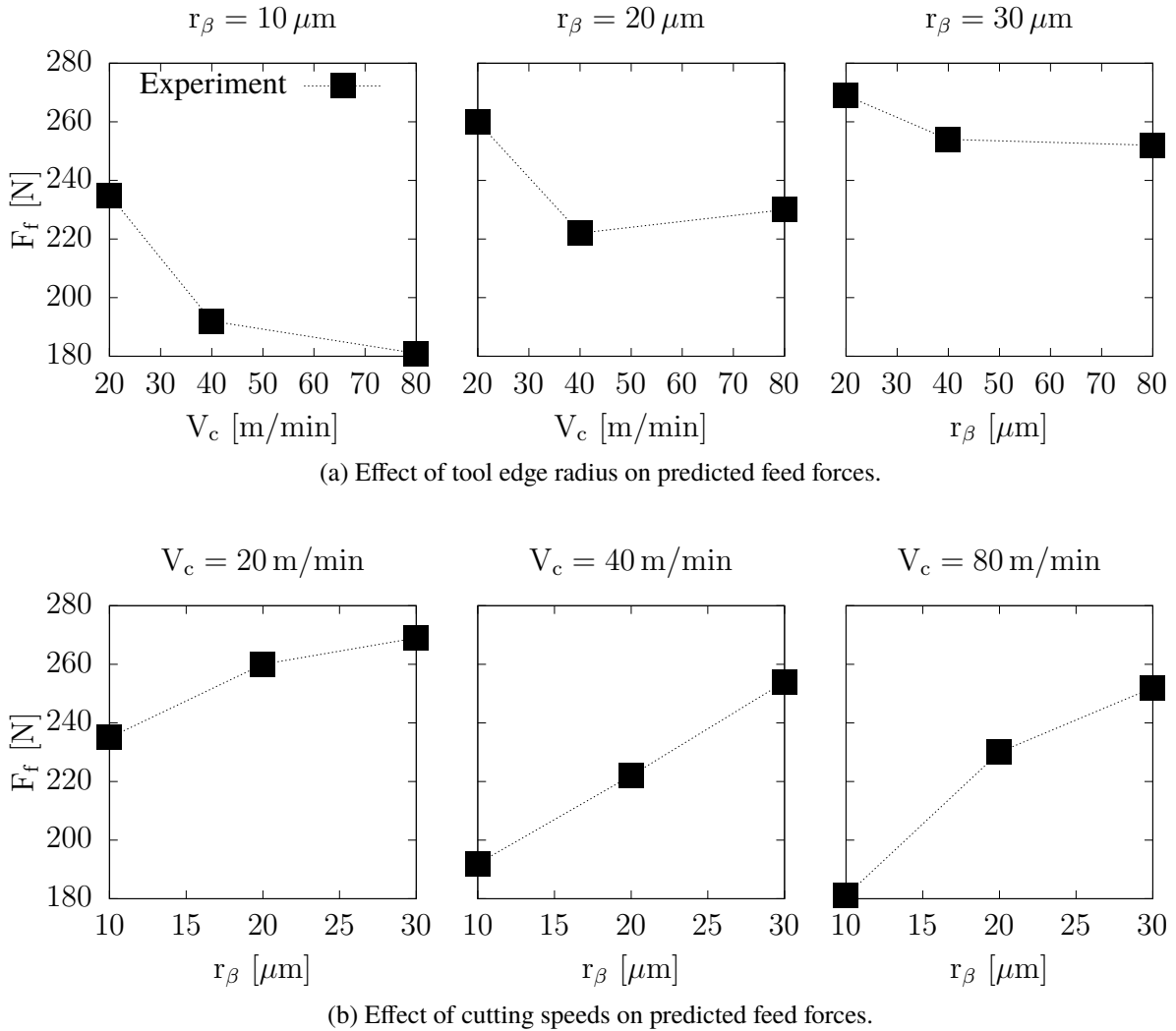


Figure 4.4: Effect of tool edge radius and cutting speed on feed forces.

4.1.3 Chip thickness and chip morphology

Chip micrographs for three different cutting speeds and two different tool edge radii are displayed in Table 4.4. The obtained chips are generally continuous with a small amount of chip serration or segmentation. This is confirmed by the chip serraⁿtion ratios displayed in Table 4.5, which is a measure that shows the level of serration or segmentation that occurs during the experimental cutting test.

The thickness of the generated chips was determined using a micrometer screw guage, by measuring points along the length of the chip with maximum thickness h_{\max} , whereas the chip serraⁿtion ratio was obtained by dividing the maximum chip thickness (h_{\max}) by the minimum chip thickness (h_{\min}), see Figure 4.6 for a graphical illustration. Each value displayed in Table

Table 4.4: Chip micrographs for three cutting speeds and two tool edge radii (courtesy of WZL).

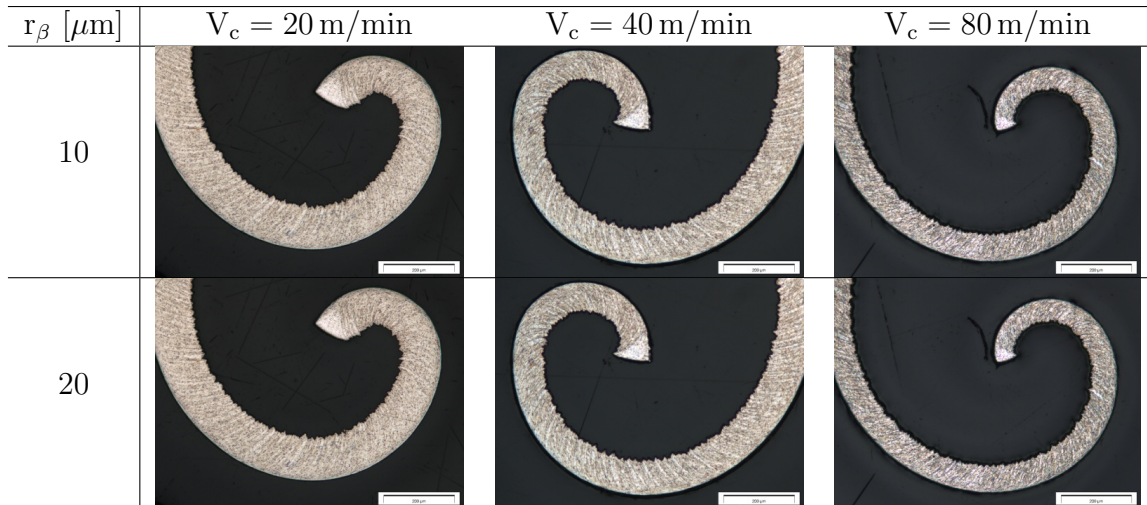


Table 4.5: Measured chip thickness and chip serration ratio

r_β [μm]	$V_c = 40 \text{ m/min}$		$V_c = 80 \text{ m/min}$	
	h_{\max} [mm]	h_{\max}/h_{\min} [-]	h_{\max} [mm]	h_{\max}/h_{\min} [-]
10	0.13	1.08	0.11	1.13
20	0.12	1.12	0.11	1.15

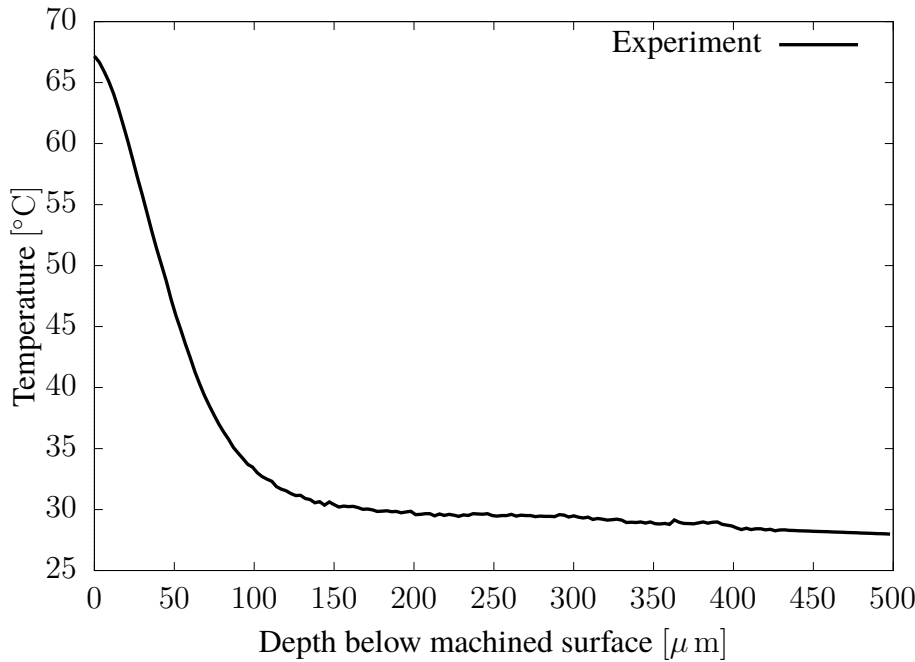


Figure 4.5: Measured temperature variation at a distance of 3.5 mm behind the tool edge up to a depth of 500 μm below machined surface.

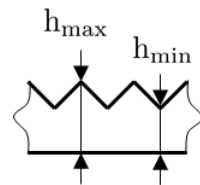


Figure 4.6: Chip serration ratio measurement illustration.

4.5 represents an average of five measurements. From the obtained results, it can be concluded that increasing cutting speeds and tool edge radius generally leads to a decrease in maximum chip thickness whereas the opposite tends to occur for chip serration.

4.2 Simulation setup

All simulations performed within this work are carried out by means of the commercial finite element software package ABAQUS/explicit.

4.2.1 Finite element model

The finite element (FE) model used throughout this work has to fulfill several basic requirements. The workpiece needs to be represented by a thermo-elasto-viscoplastic material whose mesh is able to capture large stress and strain gradients within the surface region of the workpiece as well as temperature gradients. Additionally, the mesh has to be fine enough to follow the cutting edge radius of the tool when plastic deformation occurs. To fulfill these two prerequisites, mesh density has to be sufficiently high especially in the region close to the cutting tool. Furthermore, it is important to ensure there is no significant variation in mesh density, as this will lead to a significant variation in the resolution of the calculated state variables. To check the validity of the generated mesh, a sensitivity analysis was performed by varying element sizes. For details on the sensitivity analysis, see Section 4.4.2.

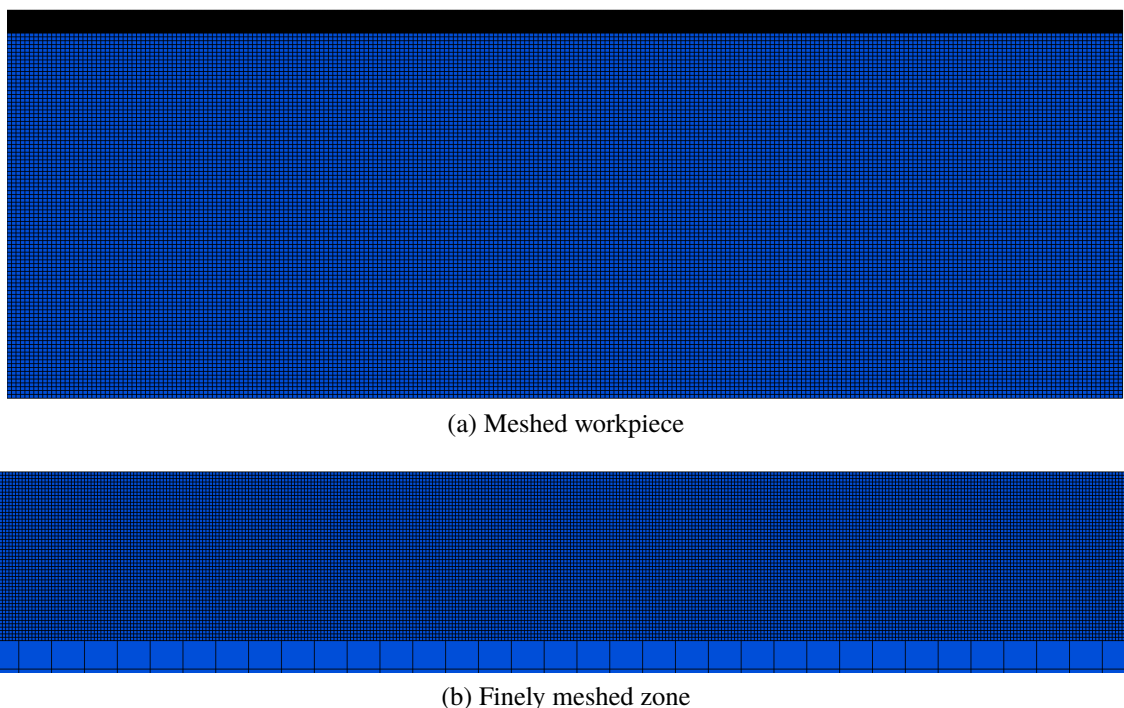


Figure 4.7: Mesh density of workpiece.

The workpiece is meshed with 148,750 4-node plane strain reduced integration bilinear displacement temperature elements (CPE4RT) available in ABAQUS/explicit. The workpiece is divided into two parts, the upper part, where most of the process significant response occur, is meshed with elements with edge lengths of $2 \mu\text{m}$ whereas the lower part, where process response are insignificant, is meshed with elements with edge lengths of $20 \mu\text{m}$. This is accomplished by dividing the workpiece into two parts, meshing both parts separately and

joining both parts at points where the nodes of the two parts coincide. The reason for this is to decrease computational effort and time, due to the fact that ABAQUS/explicit does not have adaptive remeshing capabilities. The entire workpiece has a length of 5 mm and a height of 2 mm. This dimension is chosen in order to prevent the influence of the boundary conditions on the simulated results. The finely meshed part of the workpiece has a height of 0.1 mm. Displayed in Figure 4.7 is the meshed workpiece and a magnification of part of the finely meshed region.

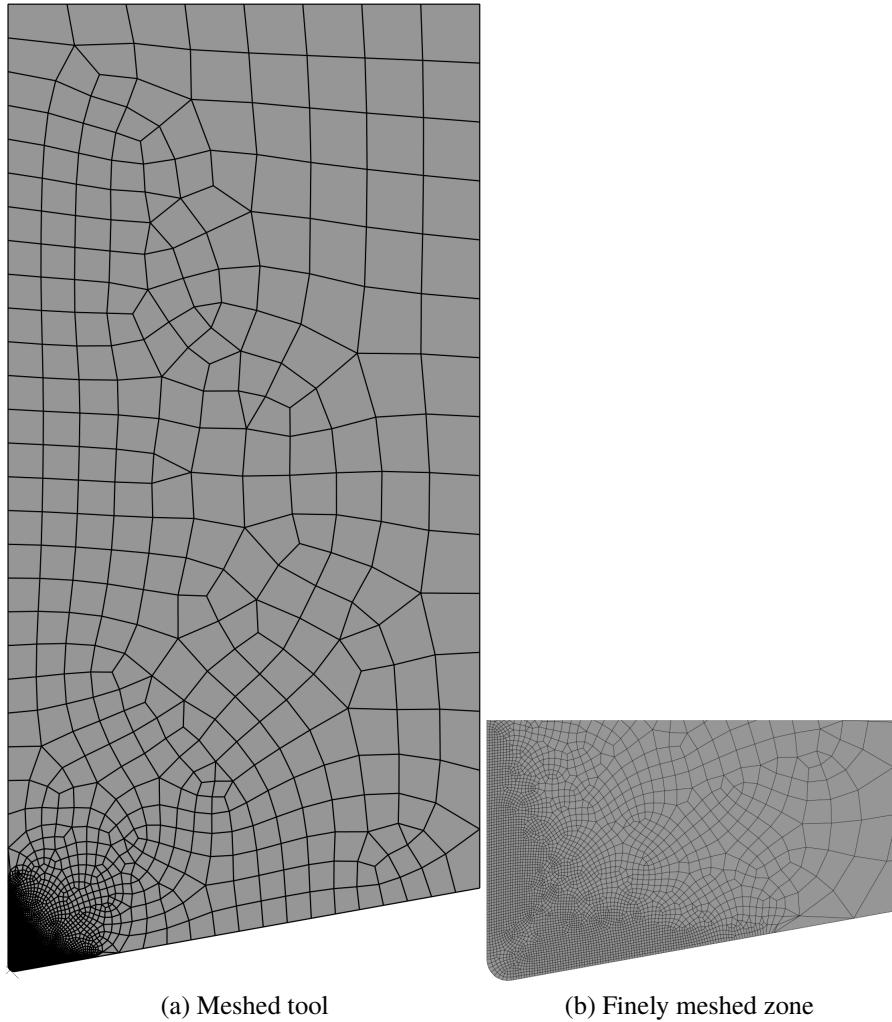


Figure 4.8: Mesh density of cutting tool.

The cutting tool is represented by a mesh also made up of a 4-node plane strain reduced integration bilinear displacement temperature element (CPE4RT) and a 3-node plane strain linear displacement temperature element (CPE3T). To make the cutting tool a rigid body, the elements are constrained to only have temperature degree of freedom. Additionally to display

the cutting tool edge radius and to also capture heat conduction in the cutting tool, the area close to the cutting edge is finely meshed with elements with edge lengths between $2.6 \mu\text{m}$ and $4 \mu\text{m}$. This fine meshing is necessary due to heat transfer by means of conduction at the boundary between workpiece and cutting tool interface. The area away from the cutting edge is coarsely meshed to save computational time. The software allows the user to create a reference point by which the movement of all the other nodes can be constrained. This allows the reference point to drive the entire cutting tool. Depicted in Figure 4.8 is the cutting tool and a magnification of the area close to the tool tip.

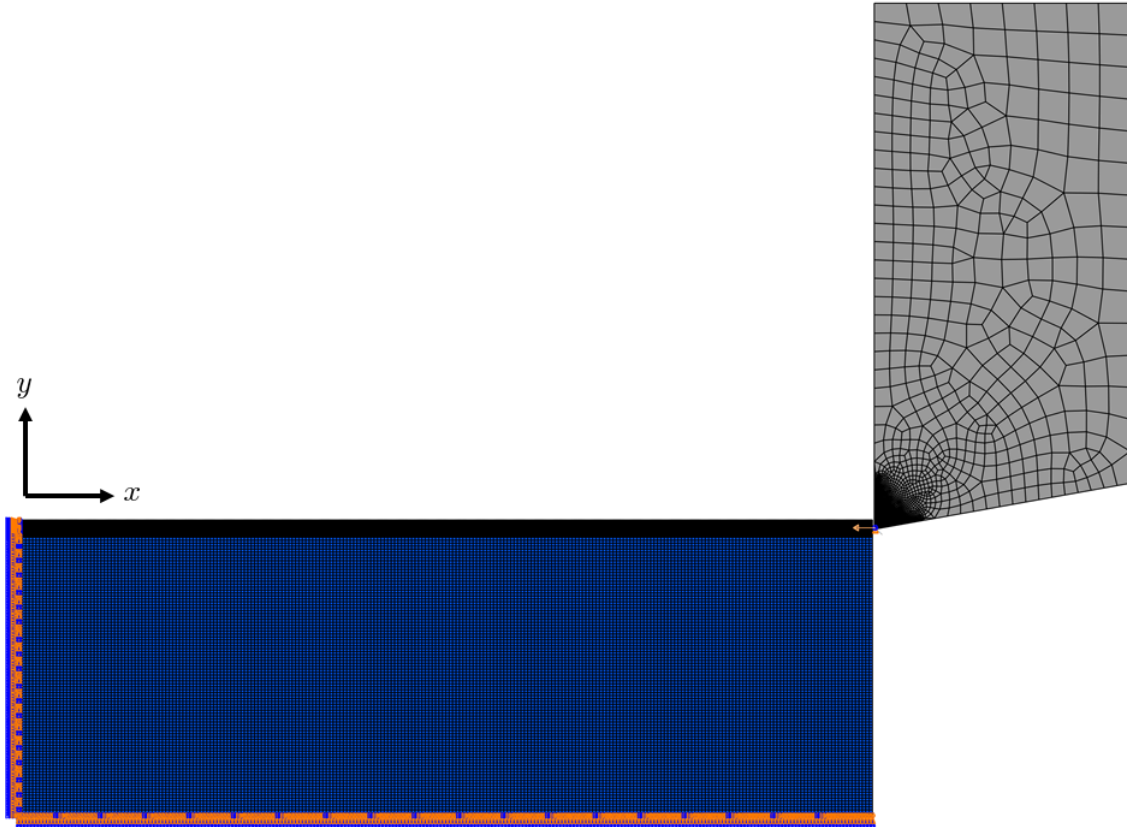


Figure 4.9: Workpiece cutting tool assembly and boundary conditions.

Also displayed in Figure 4.9 is the thermo-elasto-viscoplastic workpiece and the rigid cutting tool which moves in x-direction with a cutting velocity V_c . A penalty contact is specified between the cutting tool and the workpiece as well as the workpiece and the upper surface of the obtained chip during cutting. Contact between the workpiece and the tool is necessary to account for reaction force, without which the cutting tool will move through the workpiece without any resistance. During the simulation, the workpiece is held stationary and the cutting tool is moved relative to the workpiece. This movement occurs in small time increments which

Table 4.6: Cutting speeds and their corresponding time for a length of cut of 3mm

V_c [m/min]	Time [sec]
20	9×10^{-3}
40	4.5×10^{-3}
80	2.25×10^{-3}

can either be automatically determined by ABAQUS/explicit, based on the propagation of the speed of sound through the workpiece material, or by the user through the mass scaling option provided by ABAQUS/explicit. In this work, an automatic time step is employed. Also, the time period for the simulation has to be specified by the user. The cutting speeds and their corresponding time periods for a length of cut of 3mm are listed in Table 4.6.

4.2.2 Workpiece thermal model

The first law of thermodynamics, assuming no mass transfer or radiation, is written in the following form

$$\rho c_p \frac{\partial T}{\partial t} - \frac{\partial}{\partial x_i} \cdot \left(\lambda \frac{\partial T}{\partial x_i} \right) = \dot{q}_p, \quad (4.1)$$

where ρ is the density, c_p is the specific heat capacity and λ is the thermal conductivity. Furthermore \dot{q}_p is the heat source. Heat generation during cutting is by plastic deformation of the workpiece material. The heat generation rate \dot{q}_p due to inelastic work, which is added to the thermal energy balance is expressed as

$$\dot{q}_p = \eta_p \sigma \dot{\varepsilon}. \quad (4.2)$$

ABAQUS/explicit allows the user the possibility to alter the amount of heat generation due to plastic deformation through specification of the parameter η_p . The parameter η_p is called the Taylor-Quinney empirical constant which is often assigned a value of $\eta_p = 0.9$ Taylor and Quinney [1931]; Marusich and Ortiz [1995]. This is particularly important where the heat generated due to plastic deformation has an effect on the material behavior. This method of heat generation can be employed in an adiabatic analysis where temperature increase by inelastic deformation in the material is calculated directly at the material integration points without the need for heat conduction. It can also be used in a fully coupled thermal-stress analysis where heat conduction occurs in the workpiece material.

For heat transfer, it is assumed that the contact between the tool and chip is thermally perfect. Also the workpiece and tool boundaries away from the cutting zone are assumed to be at room

temperature ($T_\infty = 25^\circ\text{C}$). Heat loss due to convection and radiation to surroundings is not taken into account. The specific heat capacity and thermal conductivity data for IN718 are taken from DEFORM2D material library. For use in ABAQUS/explicit, the heat capacity data is converted to specific heat capacity by dividing the heat capacity data by the material density ($\rho = 8.22 \times 10^{-6}\text{Kg/mm}^3$) which is obtained from A.S.M [1997]. This is done due to the fact that DEFORM2D is based on an implicit numerical scheme which does not require the definition of the material density. The employed temperature dependent specific heat capacity c_p as well as thermal conductivity λ data are displayed in Figure 4.10. The data confirms the temperature resistive nature of IN718.

4.2.3 Workpiece mechanical model

The equation of balance of linear momentum is expressed as

$$\frac{\partial \sigma_{ij}}{\partial x_i} + b_i = \rho \frac{dv_i}{dt}, \quad (4.3)$$

where b_i and v_i denote the body force and the velocity of a particle at position x_i . The temperature dependent elastic response of the workpiece material is modeled by Hooke's law which is expressed as

$$\sigma_{ij} = C_{ijkl} (\varepsilon_{kl}^e - \alpha \Delta T \delta_{kl}), \quad (4.4)$$

where σ_{ij} is the Cauchy stress tensor, C_{ijkl} is the fourth order elastic stiffness tensor which is defined as

$$C_{ijkl} = \frac{E}{(1 + \nu)(1 - 2\nu)} \delta_{ij} \delta_{kl} + \frac{E}{(1 + \nu)} \delta_{ik} \delta_{jl} \quad (4.5)$$

and ε_{kl}^e is the elastic part of the total strain ε_{kl} which is additively decomposed into an elastic and plastic part ($\varepsilon_{kl} = \varepsilon_{kl}^e + \varepsilon_{kl}^p$). ΔT is the change in temperature and δ_{kl} is the second order identity tensor. E , ν and α are material parameters called Young's modulus, Poisson's ratio and coefficient of thermal expansion, respectively. The temperature dependent Young's modulus and Poisson's ratio are displayed in Table 4.7 whereas the coefficient of thermal expansion α is displayed in Figure 4.10. The aforementioned material data are taken from DEFORM2D material library.

To account for strain rate and temperature dependent plastic behavior of the workpiece

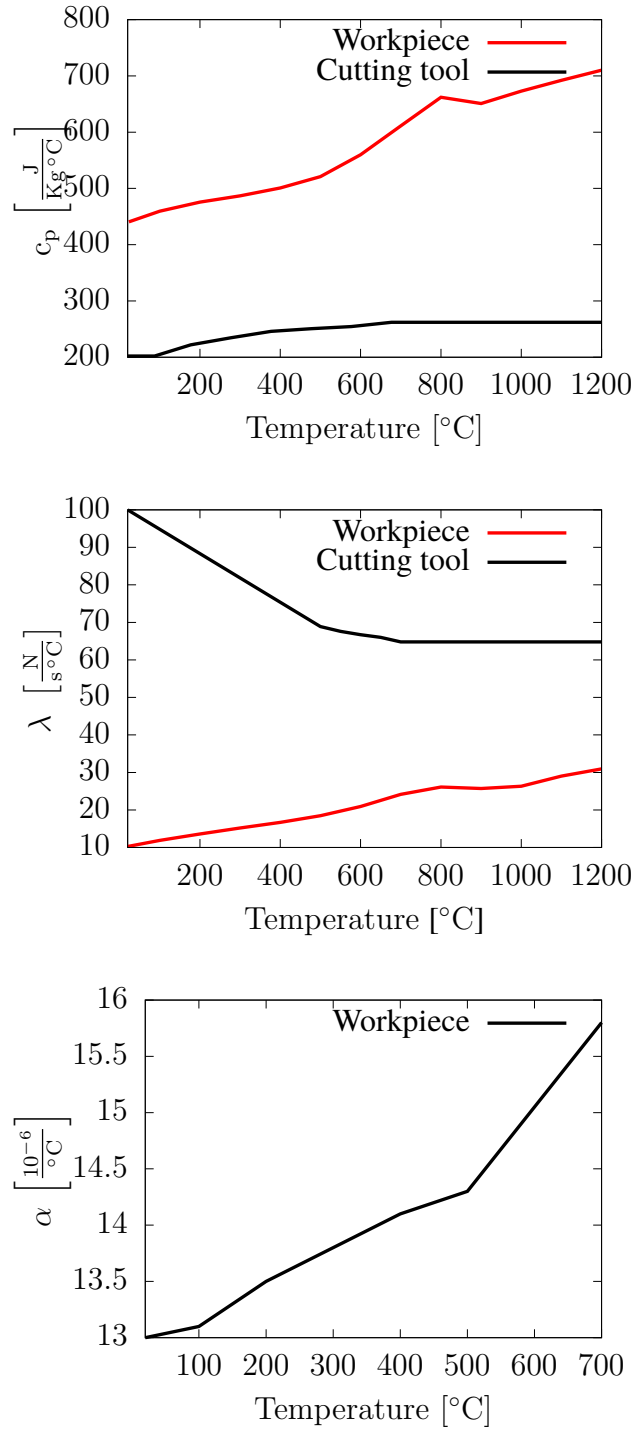


Figure 4.10: A plot of temperature dependent thermal material properties for cutting tool and IN718 workpiece.

material, the Johnson-Cook plasticity model which is expressed as

$$\underbrace{\sqrt{\frac{3}{2}} \|\sigma_{ij}^D\|}_{\sigma_{vM}} = \left(A + B \left(\underbrace{\int \|\dot{\varepsilon}_{ij}^p\| dt}_{\varepsilon} \right)^n \right) \left(1 + C \ln \left(\frac{\|\dot{\varepsilon}_{ij}^p\|}{\dot{\varepsilon}_0} \right) \right) \left(1 - \left(\frac{T - T_0}{T_m - T_0} \right)^m \right), \quad (4.6)$$

Table 4.7: IN718 mechanical material properties.

T [°C]	E [GPa]	$\nu [-]$
20	217	0.3
871	155.9	0.3

Table 4.8: Johnson-Cook flow stress material parameters for IN718 Klocke et al. [2013].

$\dot{\varepsilon}_0$ [1/sec]	T_0 [°C]	T_m [°C]	A [MPa]	B [MPa]	C [MPa]	n [-]	m [-]
10^{-3}	20	1297	1485	904	0.015	0.777	1.689

is adopted. For IN 718, different values of the coefficients (A, B, C, n, m) are available in the literature, see e.g. Singh et al. [2003]. In the current considerations, the coefficients identified by Klocke et al. [2013] are employed. Wherein, the parameters A, B and n were identified by least square fit of the first part of the Johnson-Cook model to quasi-static tensile stress-strain curves. The remaining coefficients C and m, which are responsible for strain rate and temperature effects, were obtained through inverse identification by varying C and m in cutting simulations and comparing predicted cutting force and chip geometry to experimental results. Summarized in Table 4.8 are the material parameters of the Johnson-Cook flow stress model.

To simulate chip formation, material separation during the cutting simulation has to be taken into account. As stated in Chapter 3, there are different ways by which this can be accomplished. In the current considerations, the Johnson-Cook damage model, which is based on the definition of a failure strain ε_f as a physical separation criterion, is employed. The failure strain is expressed as

$$\varepsilon_f = \left(d_1 + d_2 \exp \left(-d_3 \frac{\sigma_m}{\sigma_{vM}} \right) \right) \left(1 + d_4 \ln \left(\frac{\dot{\varepsilon}}{\dot{\varepsilon}_0} \right) \right) \left(1 + d_5 \left(\frac{T - T_0}{T_m - T_0} \right) \right), \quad (4.7)$$

where σ_m is the hydrostatic stress. The material coefficients d_i ($i = 1 \dots 5$) which are used in the simulation were identified by following the inverse method outlined in Klocke et al. [2013] for the identification of the Johnson-Cook material parameters C and m. To reduce the complexity of the parameter identification, the influence of stress triaxiality (σ_m/σ_{vM}) as well as temperature on damage are not taken into account. As a result, only d_2 and d_4 had to be identified. The identified material parameters are summarized in Table 4.9.

Table 4.9: Constants of Johnson-Cook damage model for IN718(courtesy WZL)

d_2 [-]	d_4 [-]
2.031	0.014

Table 4.10: Tungsten carbide cutting tool material properties.

ρ [Kg/mm ³]	α [10 ⁻⁶ /°C]
1.58×10^{-5}	540

4.2.4 Mechanical and thermal properties of cutting tool

The cutting tool material is tungsten carbide and is considered in the simulation as a rigid body but has the ability to conduct heat. As a result, it is important to specify thermal properties. Furthermore, the density of the cutting tool material has to be specified for conversion of heat capacity to specific heat capacity for use in an explicit finite element analysis.

Figure 4.10 shows temperature dependent convert heat capacity data to specific heat capacity data and thermal conductivity data for the cutting tool obtained from DEFORM2D material library. It shows the cutting tool material is a better heat conductor compared to Inconel 718. The rest of the tool material parameters are specified in Table 4.10.

4.2.5 Friction between tool and workpiece

As discussed in Chapter 3, a significant number of friction models are available in the literature. Within this thesis, friction between tool and workpiece is described by a Coulomb friction law and the coefficient of friction between tool and workpiece is taken as $\mu = 0.5$ for all simulations. This is due to the fact that inverse identification of the parameters of the Johnson-Cook flow stress model and shear failure model were carried out at this point. The reason for choosing the Coulomb friction model was mainly due to its availability in ABAQUS/explicit. Furthermore, many finite element models of the cutting process assume sliding in the secondary deformation zone follows a Coulomb friction model, see Markopoulos [2013] for a review. Additionally, as reported in Messner [2006], complex friction models available in the literature are tailored towards certain combinations of tool and workpiece material which implies the result predicted by such models may be different for other tool-workpiece material combinations.

Table 4.11: Comparison between simulated and experimental cutting forces.

	$V_c = 20 \text{ m/min}$		$V_c = 40 \text{ m/min}$		$V_c = 80 \text{ m/min}$	
$r_\beta [\mu\text{m}]$	$F_c^{\text{exp}} [\text{N}]$	$F_c^{\text{sim}} [\text{N}]$	$F_c^{\text{exp}} [\text{N}]$	$F_c^{\text{sim}} [\text{N}]$	$F_c^{\text{exp}} [\text{N}]$	$F_f^{\text{sim}} [\text{N}]$
10	269	285.42	234	259.83	232	254.90
20	264	286.76	233	259.73	243	257.34
30	255	291.30	245	280.06	246	262.70

Table 4.12: Comparison between simulated and experimental feed forces

	$V_c = 20 \text{ m/min}$		$V_c = 40 \text{ m/min}$		$V_c = 80 \text{ m/min}$	
$r_\beta [\mu\text{m}]$	$F_f^{\text{exp}} [\text{N}]$	$F_f^{\text{sim}} [\text{N}]$	$F_f^{\text{exp}} [\text{N}]$	$F_f^{\text{sim}} [\text{N}]$	$F_f^{\text{exp}} [\text{N}]$	$F_f^{\text{sim}} [\text{N}]$
10	235	128.09	192	113.06	181	104.74
20	260	138.65	222	118.08	230	120.82
30	269	144.94	254	144.76	252	136.41

4.3 Comparison between simulation and experiment

In this section, the predicted cutting forces, feed forces, workpiece temperature profile, chip thickness and chip morphology are compared with their corresponding experimental results. To provide a basis for comparison between simulation and experiment, simulations are carried out according to the experimental cutting schedule given in Table 4.1.

4.3.1 Cutting forces and feed forces

The simulated cutting forces (F_c^{sim}) and feed forces (F_f^{sim}) are obtained by averaging the process output forces obtained over time (see Figure 4.17 for an example of a typical curve representing the variation of process output forces with time). Table 4.11 and Figure 4.11 shows a comparison between simulated average cutting forces and experimental cutting forces. From the results, it can be observed that predicted average cutting forces are overestimated in comparison with their corresponding experimental results. The highest difference between simulated and experimental cutting forces is 14% and occurs at a cutting speed of $V_c = 20 \text{ m/min}$ and a tool edge radius of $r_\beta = 30 \mu\text{m}$. An increase in tool edge radius results in an increase in cutting forces whereas an increase in cutting speed results in a decrease in cutting forces. This trend is not observed for the experimental results. This may be due to experimental errors since an increase in cutting speed in general should lead to a decrease in frictional force between the tool and workpiece which should result in a decrease in cutting forces.

Table 4.12 and Figure 4.16 shows a comparison between simulated averaged feed forces and experimental results. The obtained simulation feed forces are underestimated in comparison

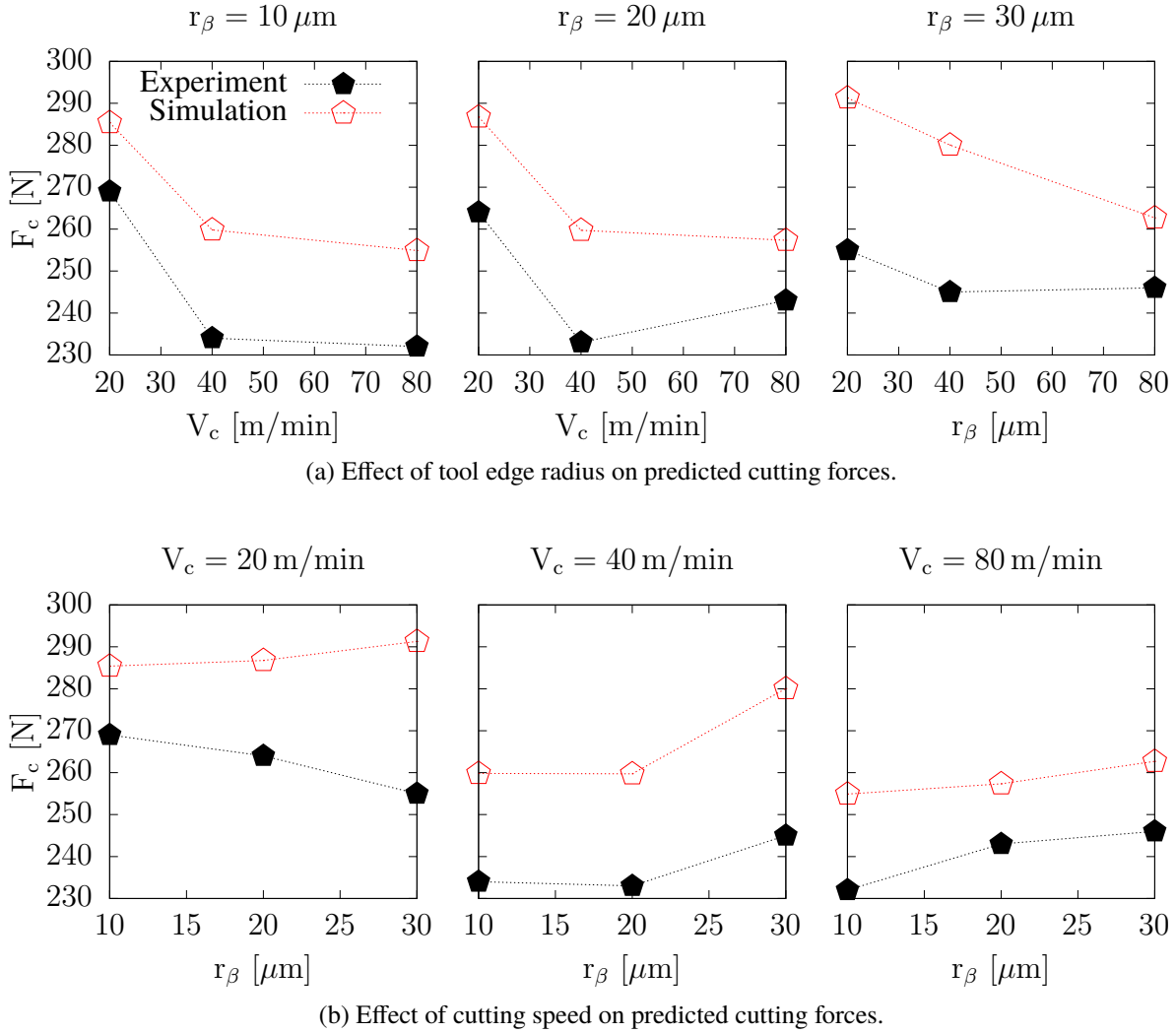


Figure 4.11: Effect of tool edge radius and cutting speed on cutting forces.

with their corresponding experimental results. A possible reason for the underestimation may be attributed to tool wear which is not accounted for in the simulations. This claim is supported by Yen et al. [2004], where simulations were performed with a chamfered and a rounded cutting tool. It was observed that by chamfering the tool edge, feed forces were significantly increased. Additionally, cutting forces were reduced as a result of the chamfer. Also simulated and experimental feed forces increase with increasing tool edge radius and generally decrease with increasing cutting speed.

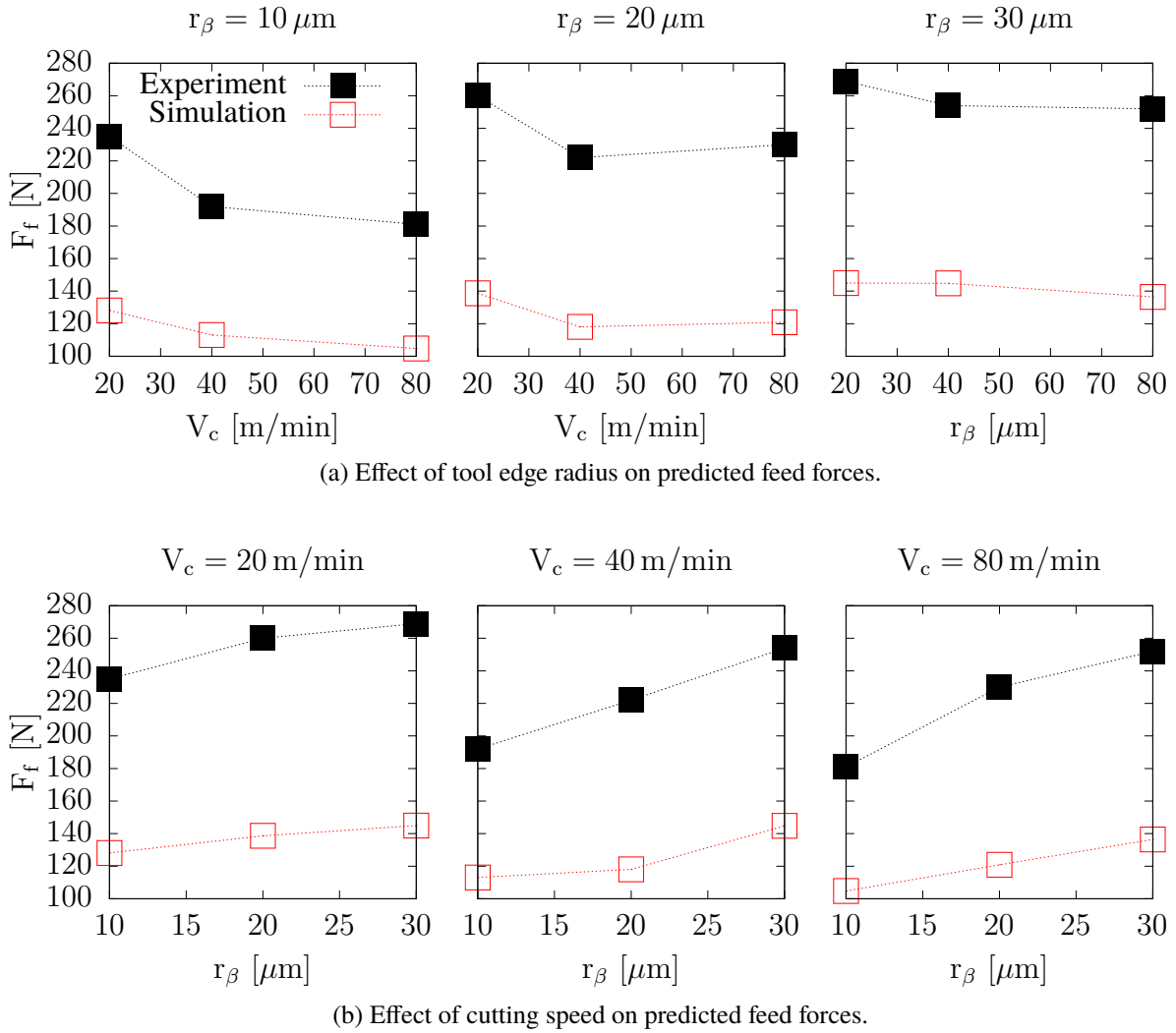


Figure 4.12: Effect of tool edge radius and cutting speed on feed forces.

4.3.2 Workpiece temperature profile

Figure 4.13 shows a plot comparing simulated temperature distribution profile measured at a distance of 3.5 mm behind the tool edge up to a depth of 500 μm and experimental temperature distribution profile measured at a distance of 4.5 mm behind the tool edge up to a depth of 500 μm using a tool edge radius of $r_\beta = 10 \mu\text{m}$ and a cutting speed of $V_c = 40 \text{ m/min}$. The reason for the discrepancy between the distance at which temperature is measured for both simulation and experiment is due to the inability to specify contact between the inner part of the cut chip and the workpiece in ABAQUS/explicit, making it difficult to simulate longer distances of cut where the curled chip touches the workpiece. The experimentally obtained temperature profile is much more localized compared to the temperature profile obtained from

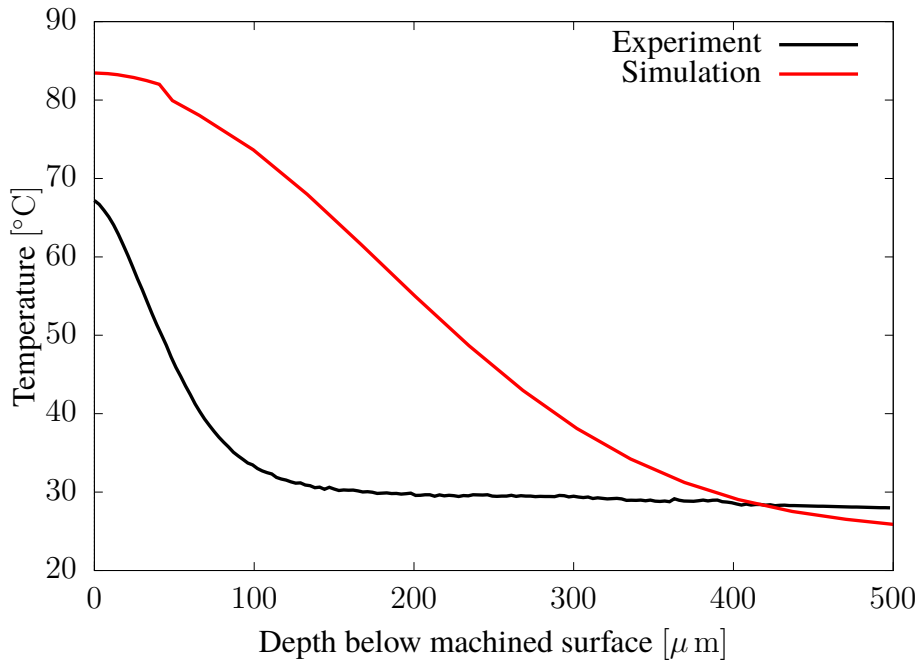


Figure 4.13: Comparison between simulated and experimental temperature measured at a distance of 3.5 mm behind the tool edge up to a depth of 500 μm .

Table 4.13: Measured chip thickness and chip serration ratio

r_β [μm]	$V_c = 40 \text{ m/min}$		$V_c = 80 \text{ m/min}$	
	h_{\max}^{\exp} [mm]	h_{\max}^{\sim} [mm]	h_{\max}^{\exp} [mm]	h_{\max}^{\sim} [mm]
10	0.13	0.079	0.11	0.074
20	0.12	0.077	0.11	0.068

simulation (see Figure 4.13). This may be as a result of the employed thermal properties of the workpiece and cutting tool material in combination with the discontinuity between the finely and coarsely meshed parts of the workpiece geometry as well as the discrepancy between the points at which temperature is measured for both simulation and experiment.

4.3.3 Chip thickness and chip morphology

Table 4.13 shows a comparison between simulated and experimental chip thickness. The general sizes of the chips predicted are underestimated with the maximum percentage difference in simulated and experimental chip thickness being 37.64% which occurs at a cutting speed of $V_c = 40 \text{ m/min}$ and a tool edge radius of $r_\beta = 10 \mu\text{m}$. The main reason for the large discrepancy between simulated and experimental chip thickness may be as a result of the fact that material separation in the simulation is achieved by element deletion. The disadvantage

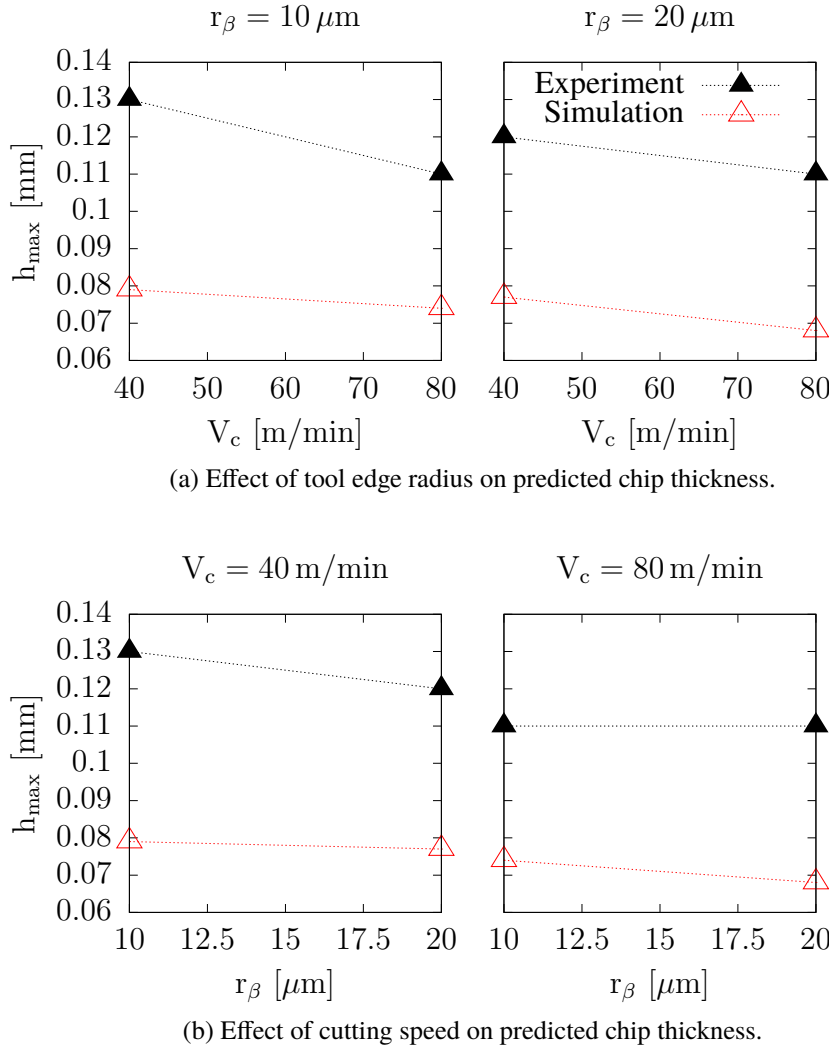
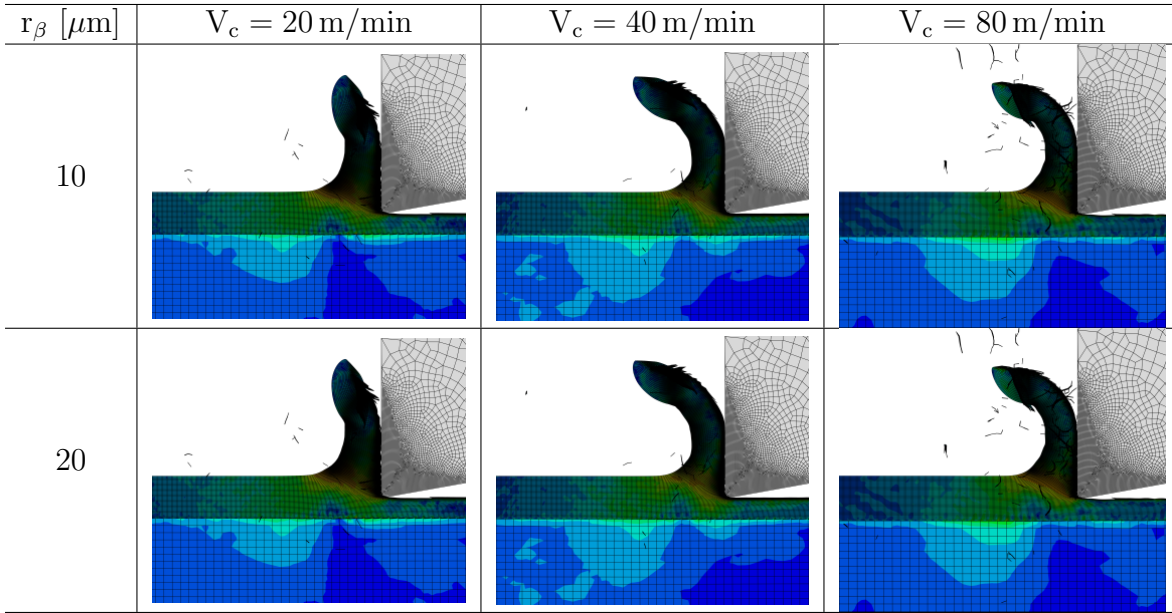


Figure 4.14: Effect of tool edge radius and cutting speed on chip thickness.

of this method of simulating material separation is the fact that the workpiece material is lost which in turn leads to a reduction in chip thickness. The difference between predicted chip thickness and experimental chip thickness is far less for models which employ remeshing in order to achieve material separation as evident in Klocke et al. [2013]. Figure 4.14 shows plots representing the effect of tool edge radius and cutting speed on predicted chip thickness. An increase in tool edge radius or cutting speed leads to a corresponding decrease in simulated chip thickness. This trend is also evident in the experimental results.

Displayed in Table 4.14 are contour plots of von-Mises stresses for two tool edge radii at three different cutting speeds. From the simulation results, it can be observed that the model at almost all combinations of cutting speeds and tool edge radii predicts a continuous chip with

Table 4.14: Predicted chip morphology for three cutting speeds and two tool edge radii.



virtually no recorded chip serration. This is not too far from the experimental results since the amount of chip serrations recorded in the experiments were very minimal with the highest serration ratio being $h_{\max}/h_{\min} = 1.15$ and occurs at a tool edge radius of $r_\beta = 20 \mu\text{m}$ and a cutting speed of $V_c = 80 \text{ m/min}$.

4.4 Discussions

In this section, the effect of friction and mesh density on predicted results as well as the parameters influencing chip serration is discussed.

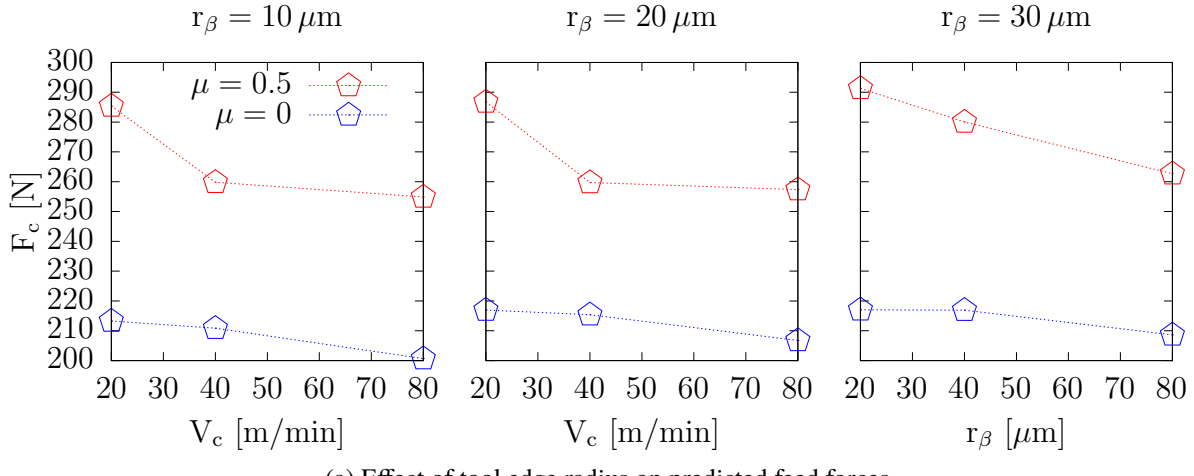
4.4.1 Influence of friction on predicted results

The simulation results presented so far are based on a Coulomb friction law with a coefficient of friction of $\mu = 0.5$. To check the influence of friction on predicted results, a second set of simulations are performed with coefficient of friction set to zero.

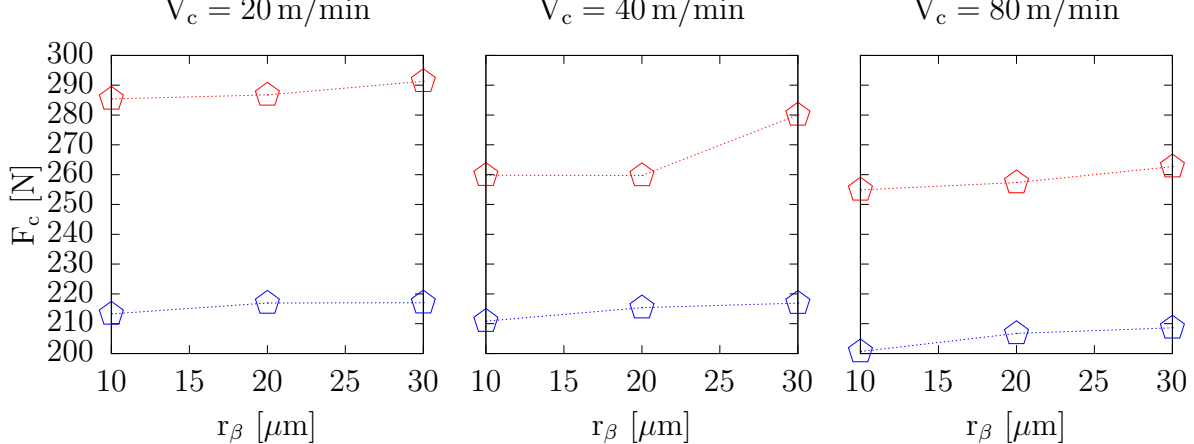
Given in Tables 4.15 and 4.16 are the predicted cutting (F_c^{sim2}) and feed forces (F_f^{sim2}) for the frictionless model and the model which accounts for friction. Also depicted in Figures 4.15 and 4.16 are plots showing the effect of friction on predicted cutting and feed forces for increasing tool edge radius and cutting speed. Without accounting for friction, predicted cutting and feed forces were underestimated for all cutting conditions. Furthermore, the cutting

Table 4.15: Comparison between simulated cutting forces for coefficient of friction $\mu = 0.5$ and $\mu = 0$.

r_β [μm]	$V_c = 20$ m/min		$V_c = 40$ m/min		$V_c = 80$ m/min	
	F_c^{sim} [N]	$F_c^{\text{sim}2}$ [N]	F_c^{sim} [N]	$F_c^{\text{sim}2}$ [N]	F_c^{sim} [N]	$F_f^{\text{sim}2}$ [N]
10	285.42	213.31	259.83	210.89	254.90	200.69
20	286.76	216.97	259.73	215.38	257.34	206.74
30	291.30	217.04	280.06	216.91	262.70	208.65



(a) Effect of tool edge radius on predicted feed forces.



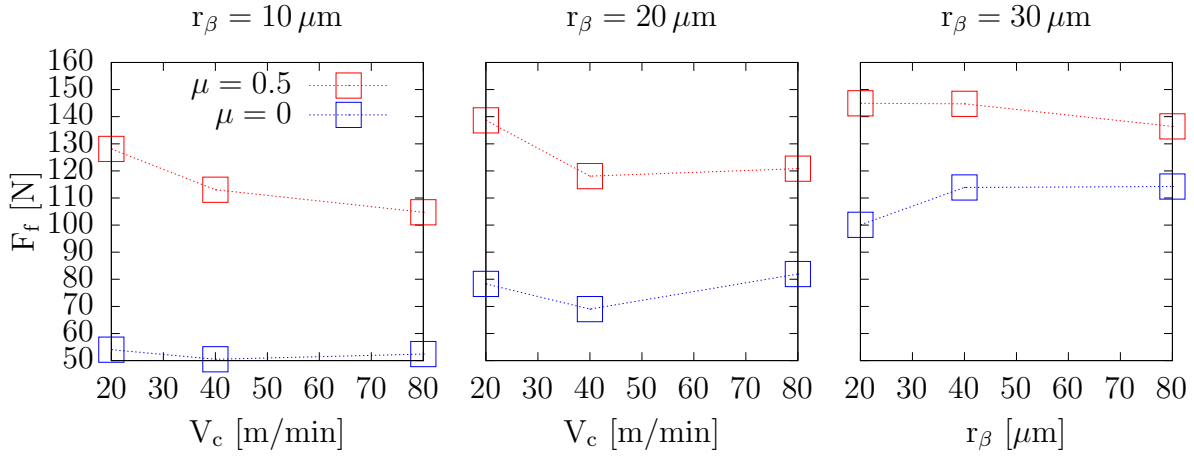
(b) Effect of cutting speed on predicted feed forces.

Figure 4.15: Effect of tool edge radius and cutting speed on cutting forces.

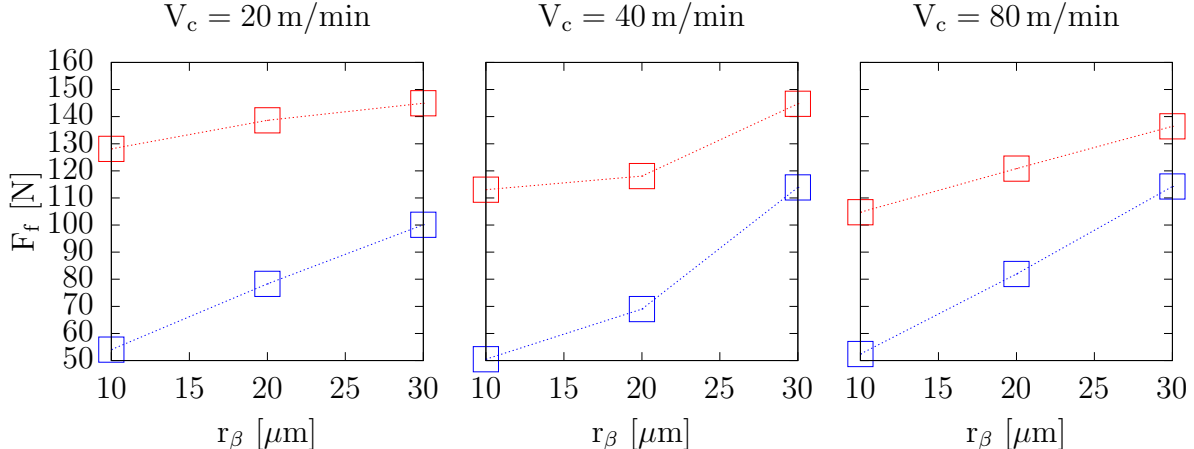
forces predicted by the frictionless model showed an increase for increasing tool edge radius and a decrease for increasing cutting speed. On the other hand, the feed forces generally showed an increase for increasing tool edge radius. However, for increasing cutting speed the

Table 4.16: Comparison between simulated feed forces for coefficient of friction $\mu = 0.5$ and $\mu = 0$.

r_β [μm]	$V_c = 20 \text{ m/min}$		$V_c = 40 \text{ m/min}$		$V_c = 80 \text{ m/min}$	
	F_f^{sim} [N]	$F_f^{\text{sim}2}$ [N]	F_f^{sim} [N]	$F_f^{\text{sim}2}$ [N]	F_f^{sim} [N]	$F_f^{\text{sim}2}$ [N]
10	128.09	54.02	113.06	50.5	104.74	52.41
20	138.65	78.3	118.08	68.99	120.82	81.92
30	144.94	100.11	144.76	113.9	136.41	114.21



(a) Effect of tool edge radius on predicted feed forces.



(b) Effect of cutting speed on predicted feed forces.

Figure 4.16: Effect of tool edge radius and cutting speed on feed forces.

result is inconclusive since increasing cutting speed did not necessarily lead to a decrease in feed force. Depicted in Figure 4.17 are plots showing change in cutting and feed force with time for friction and frictionless model.

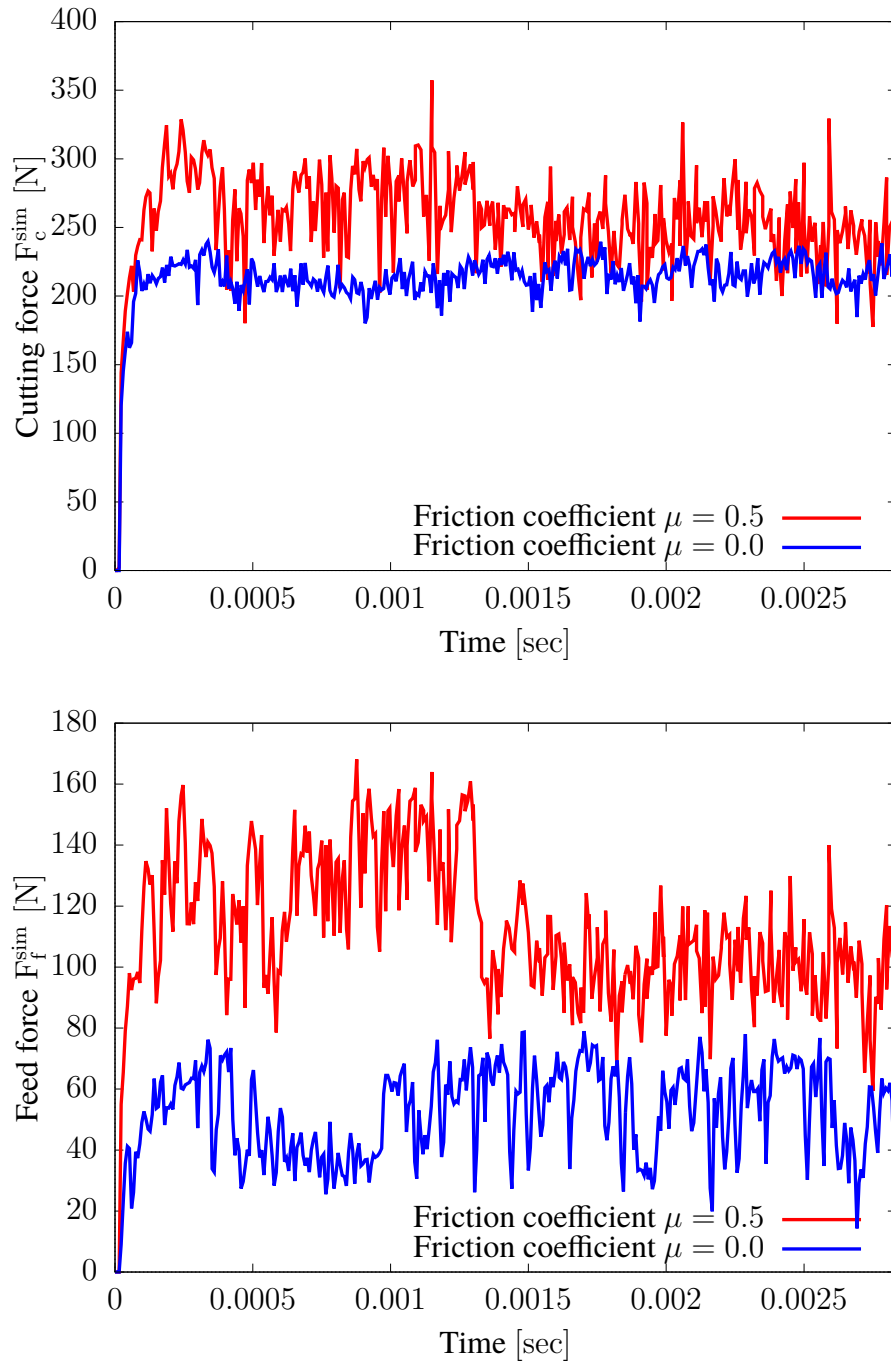
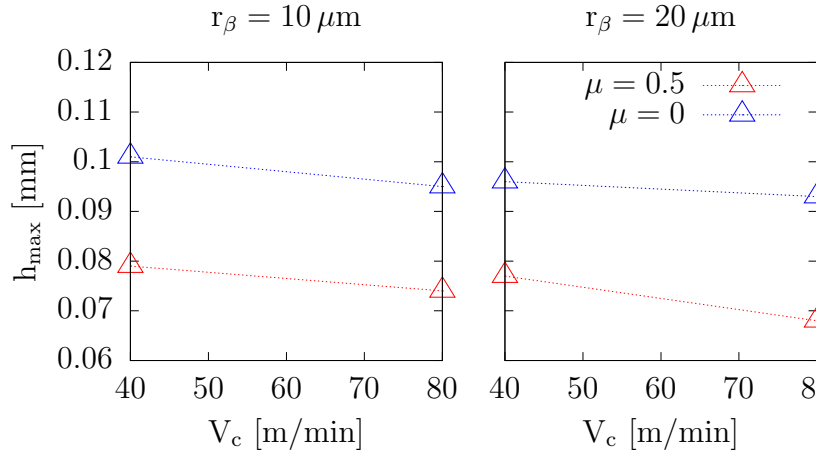


Figure 4.17: A plot representing change in cutting and feed force with time using a tool edge radius of $r_\beta = 10 \mu\text{m}$ and a cutting speed of $V_c = 40 \text{ m/min}$.

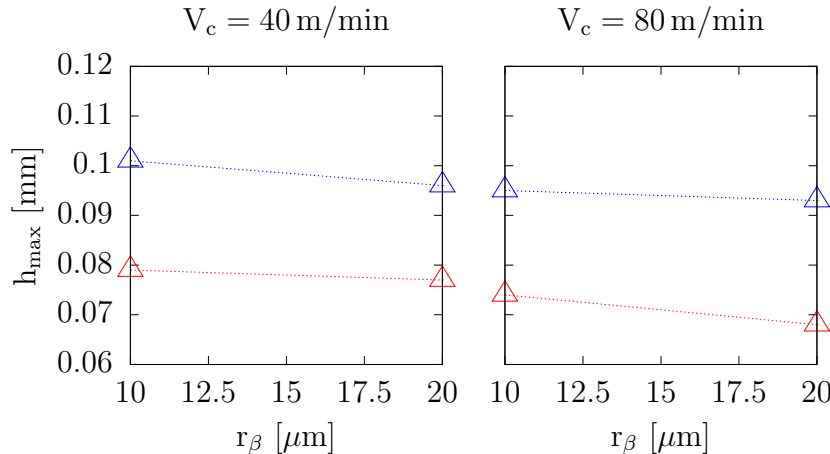
Given in Table 4.17 is a comparison between predicted chip thickness (h_{\max}^{sim2}) for frictionless model and friction model. Figure 4.18 also shows the effect of friction on predicted chip thickness for increasing tool edge radius and cutting speed. From Figure 4.18, the chip

Table 4.17: Comparison between simulated chip thicknesses for friction and frictionless model.

	$V_c = 40 \text{ m/min}$		$V_c = 80 \text{ m/min}$	
$r_\beta [\mu\text{m}]$	$h_{\max}^{\text{sim}} [\text{mm}]$	$h_{\max}^{\text{sim2}} [\text{mm}]$	$h_{\max}^{\text{sim}} [\text{mm}]$	$h_{\max}^{\text{sim2}} [\text{mm}]$
10	0.079	0.101	0.074	0.095
20	0.077	0.096	0.068	0.093



(a) Effect of tool edge radius on predicted frictionless model chip thickness.



(b) Effect of cutting speed on predicted frictionless model chip thickness.

Figure 4.18: Effect of friction on chip thickness.

thicknesses predicted by the frictionless model show an increase compared to the friction model. Furthermore, chip thicknesses predicted by the frictionless model increases with increasing tool edge radius and cutting speed. Displayed in Figure 4.19 is a comparison between the chip morphologies predicted by the frictionless and friction models. The chips predicted by both models are continuous chips without any chip serration.

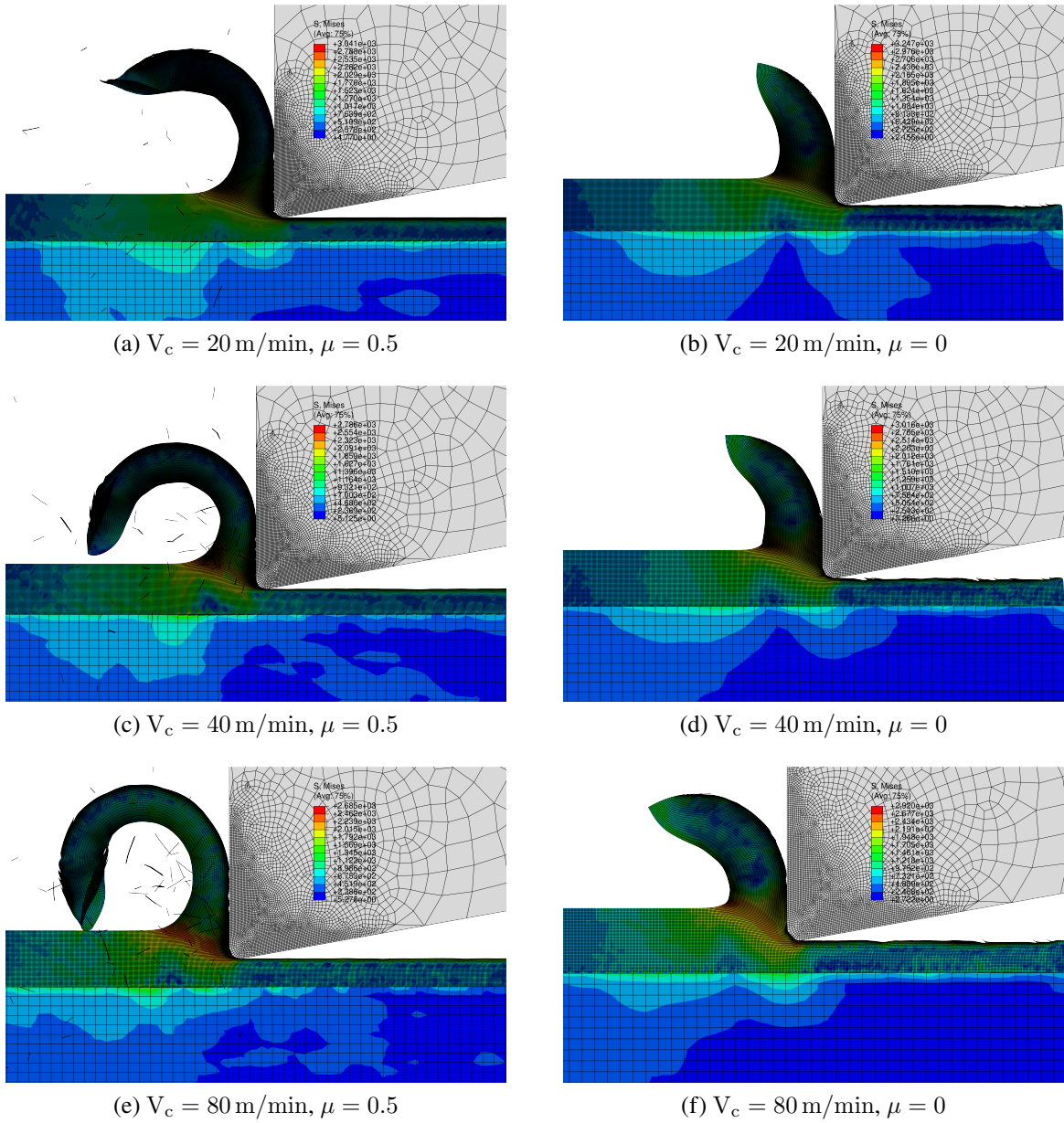


Figure 4.19: Comparison between chip morphologies for coefficient of friction $\mu = 0.5$ and $\mu = 0$ using a tool edge radius of $r_\beta = 20 \mu\text{m}$.

4.4.2 Effect of mesh density on predicted results

To check the influence of element size on simulation results, a sensitivity analysis was carried out on the mesh by performing cutting simulations for a length of cut of 0.45 mm at a cutting speed of $V_c = 40 \text{ m/min}$ and a tool edge radius of $r_\beta = 20 \mu\text{m}$ for four different mesh densities. The upper part of the workpiece is meshed with element sizes of $8 \mu\text{m}$, $4 \mu\text{m}$, $2 \mu\text{m}$ and $1 \mu\text{m}$,

and the corresponding lower part of the workpiece meshed with element sizes of $40\ \mu\text{m}$, $20\ \mu\text{m}$, $20\ \mu\text{m}$ and $10\ \mu\text{m}$, respectively. The four different meshes are depicted in Figure 4.20.

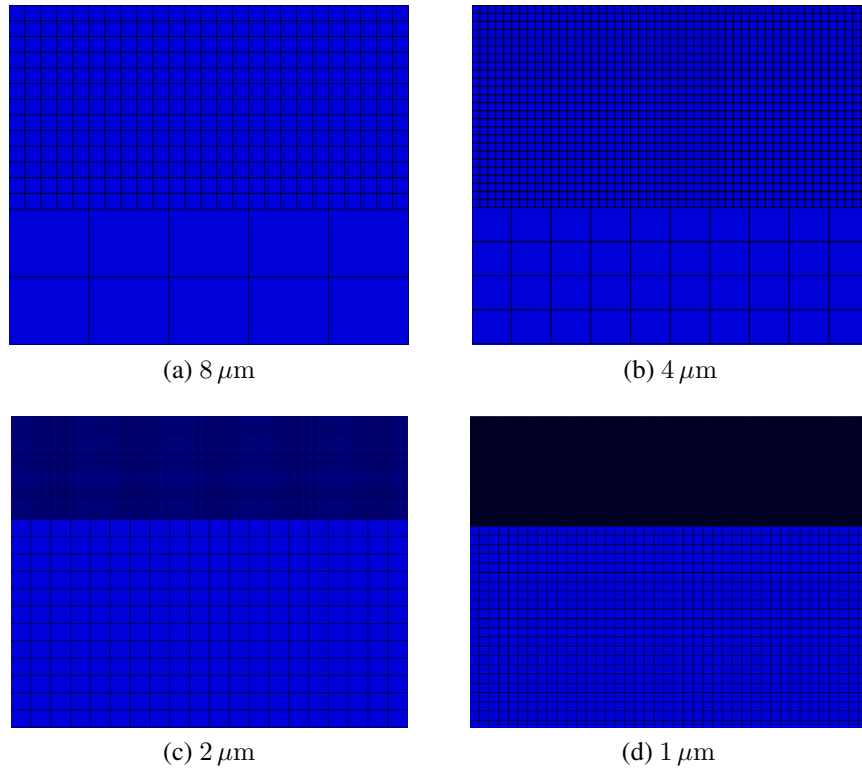


Figure 4.20: Mesh densities for sensitivity analysis.

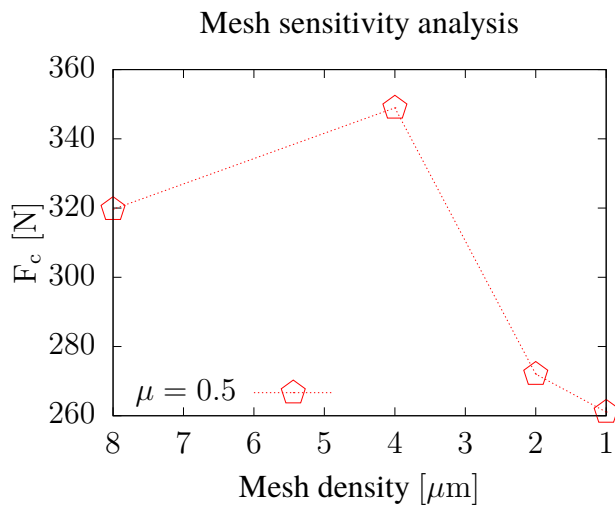


Figure 4.21: Effect of mesh density on predicted cutting forces.

Table 4.18: Predicted cutting forces for four different meshes.

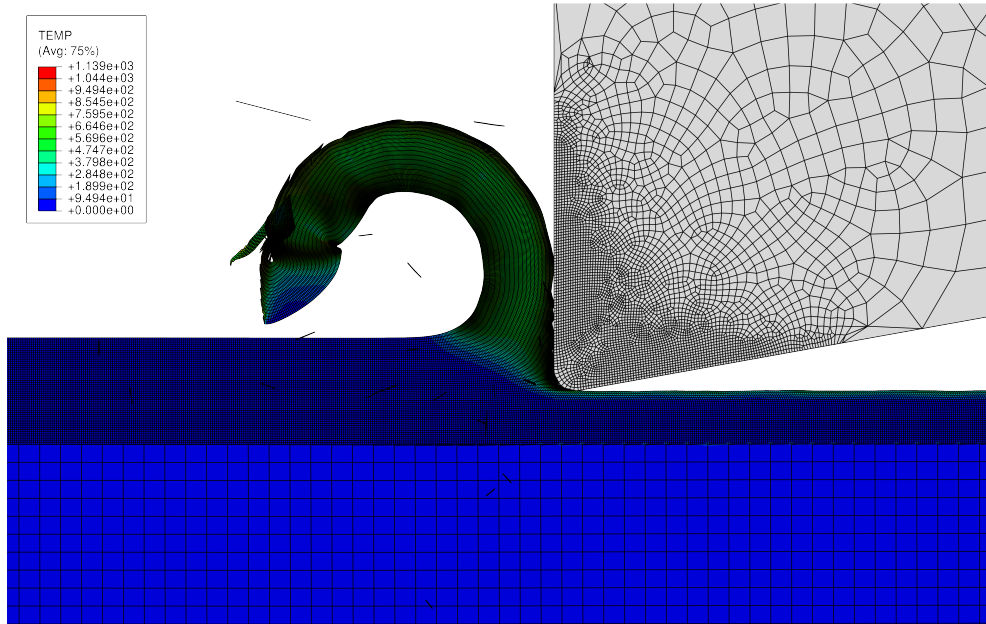
Mesh density [μm]	F_c [N]
8	319.67
4	348.93
2	272.04
1	261.07

Given in Table 4.18 and plotted in Figure 4.21 are the cutting forces predicted after performing the sensitivity analysis. The cutting forces generally decreased with increasing mesh refinement till some amount of convergence was reached. Although there still is a difference of about 4% between the cutting forces predicted by mesh $2\ \mu\text{m}$ and that predicted by mesh $1\ \mu\text{m}$, it is still fair to say there is some amount of convergence considering the effect of further mesh refinement on computational time.

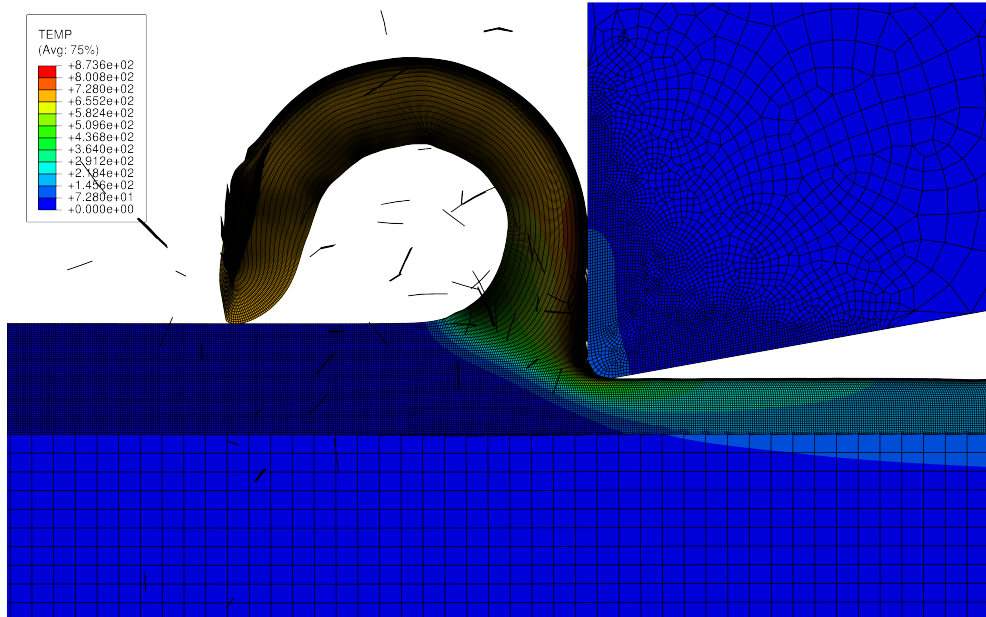
4.4.3 Parameters influencing chip serration

Although the chips obtained from experimental results showed some amount of chip serration or segmentation, the same was not the case for the chip morphologies predicted by the finite element model. To address this issue, further investigations were carried out especially concerning the precursors of serrated chip formation as stated in the literature: which are crack initiation at the free surface of the workpiece and shear localization as a result of strain softening due to thermal softening.

To check the influence of the thermophysical properties of the workpiece material on the ability of the model to predict chip serration as a result of thermal softening, simulations are carried out on two separate finite element models using a cutting tool edge radius of $r_\beta = 20\ \mu\text{m}$ and a cutting speed of $V_c = 40\text{ m/min}$. The first model is based on a fully coupled thermal stress analysis where thermal conductivity is taken into account whereas the second model is based on an adiabatic analysis where thermal conductivity is not taken into account. For the performed simulations, both models are assigned the original workpiece and tool specific heat capacity data of IN718. Temperature contour plot of the two predicted chip morphologies from these simulations are displayed in Figure 4.22. From the results, it can be observed that for both adiabatic and fully coupled thermal stress models, continuous chips are predicted. It is interesting to note that temperature profile predicted by the adiabatic model is highly localized and is mostly concentrated in the chip. This is however not the case for the fully coupled thermal stress model. Additionally, the temperature range predicted by the adiabatic model is higher than that predicted by the fully coupled thermomechanical model. Also an average



(a) Adiabatic model.

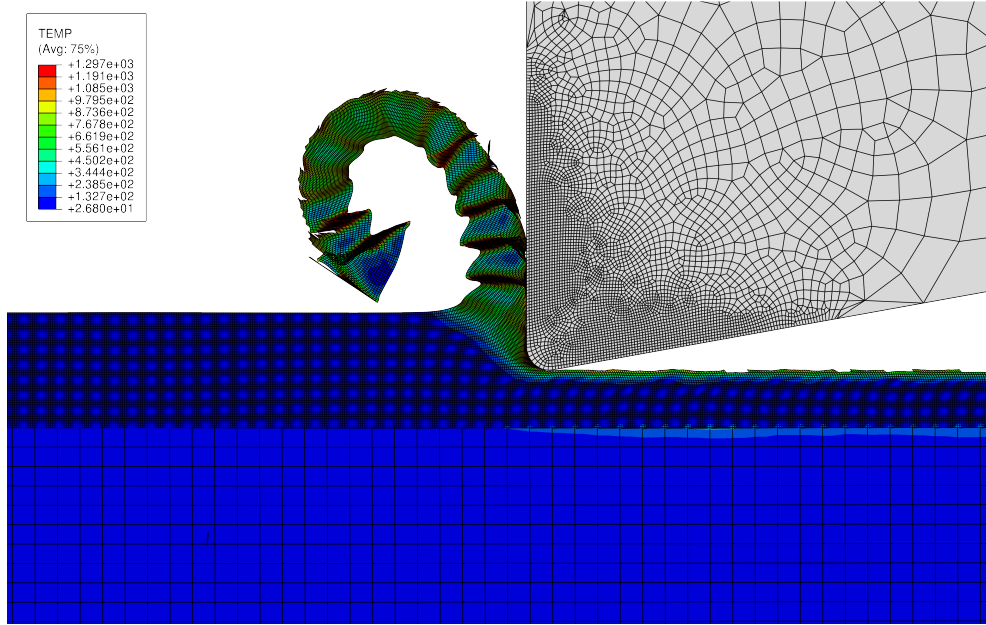


(b) Fully coupled thermal stress model.

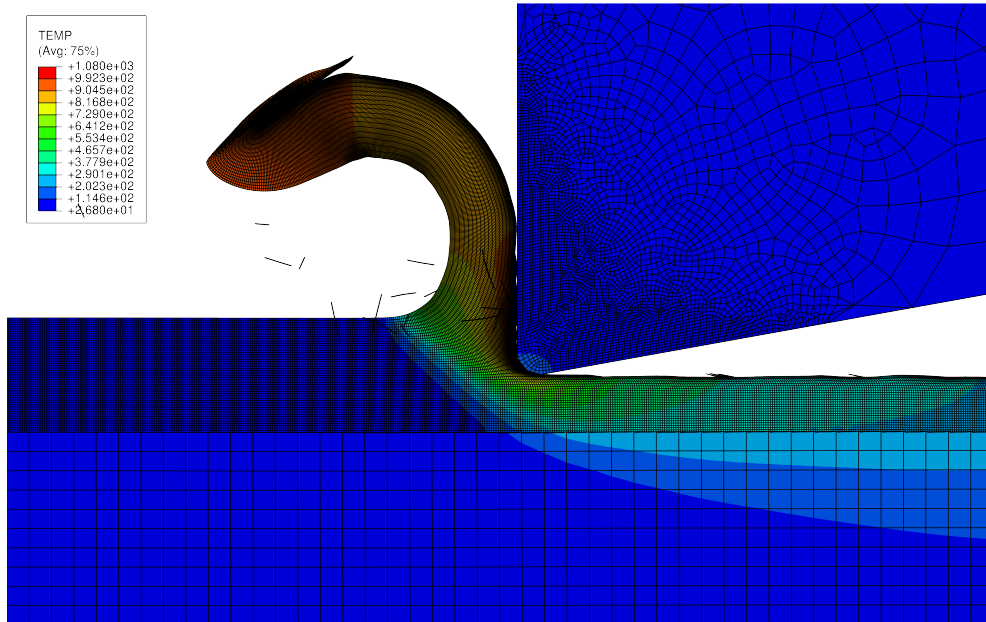
Figure 4.22: Contour plot of temperature distribution for adiabatic and fully coupled thermal model with original specific heat capacity data.

cutting force of $F_c = 218.57\text{ N}$ was predicted by the adiabatic model and $F_c = 259.72\text{ N}$ for the fully coupled thermal stress model. From the predicted chip temperatures and average cutting forces, it can be concluded that even though the adiabatic model predicted a higher

chip temperature which lead to some amount of strain softening in the primary cutting zone, the amount of heat absorbed by the chip was still not high enough to cause chip serration.



(a) Adiabatic model.



(b) Fully coupled thermal stress model.

Figure 4.23: Contour plot of temperature distribution for adiabatic and fully coupled thermal model with workpiece assigned tool specific heat capacity data.

Also, a second set of simulations are performed in which the workpiece material of both

models are assigned specific heat capacity data of the cutting tool. Contour plots of temperature for the new simulations are shown in Figure 4.23. It can be seen from the plots that by decreasing the specific heat capacity of the workpiece material, there is enough heat absorption by the workpiece material of the adiabatic model to cause plastic yielding in the primary deformation zone which in turn led to chip serration. The same observation was not made in the fully coupled thermal stress model due to a less recorded chip temperature range compared to the adiabatic model, although the temperature range predicted by both the adiabatic model and the fully coupled thermal stress model was slightly higher than the previous simulations.

From the investigations conducted, it is possible to conclude that the lack of chip serration in the finite element model is as a result of the thermophysical properties of the workpiece material, especially specific heat capacity. However, this is not the case because by reducing the specific heat capacity data of the workpiece material, the resulting cutting forces and feed forces will also be reduced due to material softening. Additionally, workpiece temperature will also be over predicted. In effect, there will be poor agreement between simulation and experimental results. What this means is that chip serration may instead be as a result of crack initiation at the free surface of the workpiece which proceeds downward along a shear plane toward the tool tip as claimed by M.C. Shaw [1993] and not adiabatic shearing as a result of material softening.

5 | Conclusions

As stated in the introduction, the need for finite element models that can accurately predict material process output parameters in order to improve the machinability of hard to machine materials, such as Inconel 718, is very important. The main objective of this thesis was to develop a finite element model of the orthogonal cutting process using ABAQUS/explicit 6.12 to predict process output parameters for Inconel 718. Although the developed model showed some agreement with experimental results, there still remain discrepancies between model predictions and experimental results.

Cutting forces predicted by the model in comparison to experimental results were overestimated for all cutting conditions with the maximum difference between predicted cutting forces and experimental cutting forces being 14%. The reason for this difference may be attributed to the right selection of coefficient of friction between the workpiece and tool interface. Predicted cutting forces generally showed an increase with increasing cutting tool edge radius and a decrease with increasing cutting speed. This trend was not observed for the experimental results and may be due to experimental errors since an increase in cutting speed in general should lead to a decrease in frictional force between tool and workpiece which in turn should lead to a decrease in cutting forces.

Feed forces predicted by the model were underestimated for all cutting conditions. The main reason for underestimation of the predicted feed forces may be attributed to the fact that tool wear is not taken into account in the simulation as shown by Yen et al. [2004]. Furthermore, predicted and experimental feed forces increased with increasing tool edge radius and generally decreased with increasing cutting speed.

Temperature predicted by the model at the machined surface of the workpiece agreed relatively well with experimental result although the experimentally obtained temperature distribution profile, measured from the machined surface up to a prescribed depth of the workpiece, showed much more localization compared to model prediction. The discrepancy may be as a result of the different points at which temperature was measured for both model and experiment due to the inability to specify contact between the inner part of the disassociated machined chip and the workpiece in ABAQUS/explicit, making it difficult to simulate longer

lengths of cut. It could also be as a result of the employed workpiece and tool thermal properties.

Chip thicknesses predicted by the model in comparison with experimental chip thicknesses were underestimated for all cutting conditions but they followed experimental trend. The reason for this underestimation was as a result of simulating workpiece separation by element deletion which resulted in a reduction in the workpiece volume. This problem may be resolved by modeling material separation using a remeshing approach. Additionally, continuous chips were predicted for all cutting conditions. This was not the case for experimental chip morphologies which showed some amount of chip serration. Furthermore, it was shown that the lack of serration in the chip morphology predicted by the finite element model may not be as a result of workpiece thermophysical data but may instead be as result of chip formation through crack propagation. This may be captured in the simulation by using damage models which account for fracture such as Cockcroft-Letham damage model as applied in Klocke et al. [2013] or the fracture model suggested by Marusich and Ortiz [1995].

Finally, by improving the contact condition between separated chip and workpiece, by applying a remeshing scheme in the model which is capable of accounting for excessive element distortion, by application of a damage model which is able to account for chip serration, by taking into account tool wear in the simulation and by improving the quality of the workpiece material data especially the thermophysical data, better agreement may be achieved between experimental results and simulation results.

List of Figures

1.1	Etched chip micrographs of Inconel 718 at cutting speeds of 50 m/min and 80 m/min (Soo et al. [2004]).	2
2.1	Interaction between tool rake face and chip (Kalhorri [2001]).	5
2.2	Orthogonal cutting depiction (Markopoulos [2013]).	6
2.3	Oblique cutting depiction (Markopoulos [2013]).	7
2.4	Locations of the deformation zones in two dimensional orthogonal cutting (Tönshoff [1995]).	8
2.5	Types of chips produced in metal cutting (Kalhorri [2001]).	10
2.6	Piispanen's deck of cards model (V.Piispanen [1948]).	10
2.7	Illustration of Merchant's circle (Markopoulos [2013]).	11
2.8	Illustration of Lee and Shaffer's slip-line theory for orthogonal cutting (Markopoulos [2013]).	14
2.9	Zerov's qualitative model on the left and simplified model on the right (Markopoulos [2013]).	16
3.1	Example of a two dimensional finite element mesh with linear triangular elements, discretization of a turbine blade Huebner and Thornton [1982]. . . .	20
3.2	Finite element formulations Roll and Tekkaya [1993]	24
3.3	Split Hopkinson Pressure Bar setup (Lee and Lin [1998]).	27
3.4	Normal and frictional stress distribution along the rake face as suggested by Zorev [1963]	32
3.5	An illustration of a geometrical node separation (Klocke [n.d.]).	33
3.6	Cockcroft and Letham damage criterion for the prediction of serrated chip formation; (a) flow stress reduction Klocke et al. [2013]; (b) element deletion and element rough edge smoothing Umbrello [2008].	35
3.7	Material separation as a result of remeshing Klocke [n.d.].	36
3.8	Refined finite element mesh based on a combination of plastic work rate and displacement gradient Kalhorri [2001].	37

4.1	Setup for orthogonal cutting test (courtesy WZL).	41
4.2	Setup for the determination of the machined surface temperature (courtesy WZL).	42
4.3	Effect of tool edge radius and cutting speed on feed forces.	44
4.4	Effect of tool edge radius and cutting speed on feed forces.	45
4.5	Measured temperature variation at a distance of 3.5 mm behind the tool edge up to a depth of 500 μm below machined surface.	47
4.6	Chip serration ratio measurement illustration.	47
4.7	Mesh density of workpiece.	48
4.8	Mesh density of cutting tool.	49
4.9	Workpiece cutting tool assembly and boundary conditions.	50
4.10	A plot of temperature dependent thermal material properties for cutting tool and IN718 workpiece.	53
4.11	Effect of tool edge radius and cutting speed on cutting forces.	57
4.12	Effect of tool edge radius and cutting speed on feed forces.	58
4.13	Comparison between simulated and experimental temperature measured at a distance of 3.5 mm behind the tool edge up to a depth of 500 μm	59
4.14	Effect of tool edge radius and cutting speed on chip thickness.	60
4.15	Effect of tool edge radius and cutting speed on cutting forces.	62
4.16	Effect of tool edge radius and cutting speed on feed forces.	63
4.17	A plot representing change in cutting and feed force with time using a tool edge radius of $r_\beta = 10 \mu\text{m}$ and a cutting speed of $V_c = 40 \text{ m/min}$	64
4.18	Effect of friction on chip thickness.	65
4.19	Comparison between chip morphologies for coefficient of friction $\mu = 0.5$ and $\mu = 0$ using a tool edge radius of $r_\beta = 20 \mu\text{m}$	66
4.20	Mesh densities for sensitivity analysis.	67
4.21	Effect of mesh density on predicted cutting forces.	67
4.22	Contour plot of temperature distribution for adiabatic and fully coupled thermal model with original specific heat capacity data.	69
4.23	Contour plot of temperature distribution for adiabatic and fully coupled thermal model with workpiece assigned tool specific heat capacity data.	70

List of Tables

1.1	Nominal composition of IN 718 A.S.M [1997]	1
3.1	Overview of common element shapes, the corresponding nodal position and the degree of the shape function (Knothe and Wessels [1992]).	20
4.1	Experimental plan for cutting test	43
4.2	Experimentally obtained cutting and feed forces at all three combinations of cutting speed and cutting edge radii	43
4.3	Measured temperature close to the machined surface for three different cutting speeds with a tool edge radius of $r_\beta = 10 \mu\text{m}$	43
4.4	Chip micrographs for three cutting speeds and two tool edge radii (courtesy of WZL).	46
4.5	Measured chip thickness and chip serration ratio	46
4.6	Cutting speeds and their corresponding time for a length of cut of 3mm . . .	51
4.7	IN718 mechanical material properties.	54
4.8	Johnson-Cook flow stress material parameters for IN718 Klocke et al. [2013].	54
4.9	Constants of Johnson-Cook damage model for IN718(courtesy WZL)	55
4.10	Tungsten carbide cutting tool material properties.	55
4.11	Comparison between simulated and experimental cutting forces.	56
4.12	Comparison between simulated and experimental feed forces	56
4.13	Measured chip thickness and chip serration ratio	59
4.14	Predicted chip morphology for three cutting speeds and two tool edge radii. .	61
4.15	Comparison between simulated cutting forces for coefficient of friction $\mu = 0.5$ and $\mu = 0$	62
4.16	Comparison between simulated feed forces for coefficient of friction $\mu = 0.5$ and $\mu = 0$	63
4.17	Comparison between simulated chip thicknesses for friction and frictionless model.	65
4.18	Predicted cutting forces for four different meshes.	68

Bibliography

- A.S.M [1997], *in* J. Davis, ed., ‘ASM International: Heat resistance metals’.
- Astakhov, V. [2005], ‘On the inadequacy of the single-shear plane model of chip formation’, *International Journal of Mechanical Sciences* **47**, 1649 – 1672.
- Bäker, M. [2004], *in* ‘Finite element simulation of chip formation, Habilitation, TU Braunschweig’.
- Bäker, M., Rösler, J. and Siemers, C. [2002], ‘A finite element model of high speed metal cutting with adiabatic shearing’, *Computers and Structures* **80**, 495 – 513.
- Bathe, K. [1996], *in* ‘Finite element procedures’, Englewood Cliffs.
- Bayoumi, H. and Gadala, M. [2004], ‘A complete finite element treatment for the fully coupled implicit ale formulation’, *Computational Mechanics* **33**, 435 – 452.
- Childs, T. [2009], ‘Modelling orthogonal machining of carbon steels. part i: Strain hardening yield delay effects’, *International Journal of Mechanical Sciences* **51**, 402 – 411.
- Childs, T. and Maekawa, K. [1990], ‘Computer-aided simulation and experimental studies of chip flow and tool wear in the turning of low alloy steels by cemented carbide tools’, *Wear* **139**, 235 – 250.
- Childs, T., Otieno, A. and Maekawa, K. [1994], The influence of material flow properties on the machining of steels, *in* ‘Proceedings of the 3rd international conference on the behaviour of materials in machining’, pp. 104– 119.
- Childs, T. and Rahmad, R. [2009a], ‘The effect of a yield drop on chip formation of soft carbon steels’, *Machining Science and Technology* **13**, 471 – 487.
- Childs, T. and Rahmad, R. [2009b], ‘Modelling orthogonal machining of carbon steels. part ii: Comparisons with experiments’, *International Journal of Mechanical Sciences* **51**, 465 – 472.

- Chung, W., Cho, J. and Belytschko, T. [1998], ‘On the dynamic effects of explicit fem in sheet metal forming analysis’, *Engineering Computations* **15**, 750 – 776.
- Cockcroft, M. and Latham, D. [1968], ‘Ductility and workability of metals’, *Journal of the Institute of Metals* **96**, 33 – 39.
- Crisfield, M. [1997], in ‘Non-linear finite element of solid and structures’, Vol. 2, John Wiley and sons.
- Dewhurst, P. [1978], ‘On the non-uniqueness of the machining process’, *Proceedings of the Royal Society London A* **360**, 587 – 610.
- Ernst, H. and Merchant, M. [1941], ‘Chip formation, friction and high quality machined surfaces’, *Surface treatment of metals issue, American Society for Metals* **29**, 299 – 378.
- Gordon, M. [1967], ‘The applicability of the binomial law to the process of friction in the cutting of metals’, *Wear* **10**, 274 – 290.
- Gregory, K. [2003], ‘Failure modelling of titanium 6al-4v and aluminum 2024-t3 with the johnson-cook material model’, *National Technical Information Service Report* .
- Hoppe, S. [2003], in ‘Experimental and numerical analysis of chip formation in metal cutting, PhD dissertation, RWTH Aachen University’.
- Huang, J. and Black, J. [1996], ‘An evaluation of chip separation criteria for the fem simulation of machining’, *Journal of Manufacturing Science and Engineering* **118**, 545 – 554.
- Huebner, K. and Thornton, E. [1982], in ‘The Finite Element Method for Engineers’, John Wiley and Sons.
- Hyun, S. and Lindgren, L. [2001], ‘Smoothing and adaptive remeshing schemes for graded element’, *International Journal for Numerical Methods in Biomedical Engineering* **17**, 1 – 17.
- Jaspers, S. and Dautzenberg, J. [2002], ‘Material behaviour in metal cutting: strains, strain rates and temperatures in chip formation’, *Journal of Material Processing Technology* **121**, 123– 135.
- Johnson, G. and Cook, W. [1983], A constitutive model and data for metals subjected to large strains, high strain rates and high temperatures, in ‘Proceedings of the 7th international symposium on ballistics’, pp. 541– 54.

- Johnson, G. and Cook, W. [1985], ‘Fracture characteristics of three metals subjected to various strains, strain rates, temperatures and pressures’, *Engineering Fracture Mechanics* **21**, 31 – 48.
- Kalhori, V. [2001], *in ‘Modelling and simulation of mechanical cutting*, PhD dissertation, Lulea University of Technology’.
- Klocke, F. [n.d.], *in ‘Simulation techniques in manufacturing technology, Lecture notes’*.
- Klocke, F., Buchkremer, S. and Lung, D. [2013], ‘Inverse identification of the constitutive equations of in 718 and aisi 1045 from fe machining simulations’, *Procedia CIRP* **8**, 212–217.
- Knothe, K. and Wessels, H. [1992], *in ‘Finite Elemente - Eine Einführung für Ingenieure’*, Springer Verlag.
- Kobayashi, S., Oh, S. and Altan, T. [1989], *in ‘Metal forming and the finite element method’*, Oxford University Press.
- Kudo, H. [1965], ‘Some new slip-line solutions for two-dimensional steady-state machining’, *International Journal of Mechanical Sciences* **7**, 43 – 55.
- Lee, E. and Schaffer, B. [1951], ‘The theory of plasticity applied to a problem of machining’, *Journal of Applied Mechanics* **18**, 405 – 413.
- Lee, W. and Lin, C. [1998], ‘High-temperature behavior of ti6al4v alloy evaluated by high strain-rate compression tests’, *Journal of Material Processing Technology* **75**, 127 – 135.
- Lin, Z. and Lin, S. [1992], ‘A coupled finite element model of thermo-elastic-plastic large deformation for orthogonal cutting’, *Journal of Engineering Materials and Technology* **114**, 218 – 226.
- Madhavan, V., Chandrasekar, S. and Farris, T. [1998], ‘Machining as a wedge indentation’, *Journal of Applied Mechanics* **67**, 128– 139.
- Markopoulos, A. [2013], *in ‘Finite element method in machining processes’*, Springer, London.
- Marusich, T. and Ortiz, M. [1995], ‘Modelling and simulation of high-speed machining’, *International Journal for Numerical Methods in Engineering* **38**, 3675 – 3695.
- M.C. Shaw, A. V. [1993], ‘Chip formation in the machining of hardened steel’, *CIRP Annals* **42**, 29 – 33.

- Merchant, M. [1945], ‘Mechanics of the metal cutting process. ii. plasticity conditions in orthogonal cutting’, *Journal of Applied Physics* **16**, 318 – 324.
- Messner, G. [2006], in ‘Modelling Metal Cutting Processes under Consideration of Elastic Material Properties’, PhD dissertation, RWTH Aachen University’.
- Meyer, H. and Kleponis, D. [2001], ‘Modelling the high strain rate behaviour of titanium undergoing ballistic impact and penetration’, *International Journal of Impact Engineering* **26**, 509 – 521.
- Nakayama, K., Arai, M. and Kanda, T. [1988], ‘Machining characteristics of hard materials’, *CIRP Annals* **37**, 89 – 92.
- Obikawa, T., Sasahara, H., Shirakashi, T. and Usui, E. [1997], ‘Application of computational machining methods to discontinuous chip formation’, *Journal of Manufacturing Science and Engineering* **119**, 667 – 674.
- Obikawa, T. and Usui, E. [1996], ‘Computational machining of titanium alloy–finite element modeling and a few results’, *Journal of Manufacturing Science and Engineering* **118**, 208 – 215.
- Owen, D. and Jr., M. V. [1999], ‘Computational techniques applied to high-speed machining under adiabatic strain localization conditions’, *Computer Methods in Applied Mechanics and Engineering* **171**, 445 – 461.
- Oxley, P. [1989], in ‘The mechanics of machining: an analytical approach to assessing machinability’, Halsted Press, New York.
- Rahman, M., Seah, W. and Teo, T. [1997], ‘The machinability of inconel 718’, *Journal of Material Processing Technology* **63**, 199 – 204.
- Reddy, J. [1993], in ‘Introduction to the Finite Element Method’, McGraw-Hill.
- Roll, K. and Tekkaya, A. [1993], Numerische verfahren der prozesssimulation in der umformtechnik, in ‘Umformtechnik Handbuch für Industrie und Wissenschaft’, Vol. 4, Springer.
- Runnemalm, H. and Hyun, S. [2000], ‘Three dimensional welding analysis using adaptive mesh scheme’, *Computer Methods in Applied Mechanics and Engineering* **189**, 515 – 523.
- Sekhon, G. and Chenot, J. [1993], ‘Numerical simulation of continuous chip formation during non-steady orthogonal cutting’, *Engineering Computations* **10**, 31 – 48.

- Shatla, M., Kerk, C. and Altan, T. [2001a], ‘Process modeling in machining. part i: determination of flow stress data’, *International Journal of Machine Tools and Manufacture* **41**, 1511–1534.
- Shatla, M., Kerk, C. and Altan, T. [2001b], ‘Process modeling in machining. part ii: validation and applications of the determined flow stress data’, *International Journal of Machine Tools and Manufacture* **41**, 1659–1680.
- Shirakashi, T., Maekawa, K. and Usui, E. [1983], ‘Flow stress of low carbon steel at high temperature and strain rate’, *Bulletin of the Japan Society of Precision Engineering* **17**, 161–166.
- Singh, K., Hamann, A., Klingbeil, D., Sievert, R., Künecke, G., Clos, R., Schreppel, U. and Veit, P. [2003], ‘Versagenssimulation dynamisch belasteter Proben mit unterschiedlichen mehrachsigen Zuständen unter Verwendung des Johnson-Cook-Versagensmodells für eine Nickelbasislegierung’, *Technische Mechanik* **23**, 205 – 215.
- Soo, S., Aspinwall, D. and Dewes, R. [2004], ‘3d fe modelling of the cutting of inconel 718’, *Journal of Materials Processing Technology* **150**, 116 – 123.
- Taylor, G. and Quinney, H. [1931], ‘The plastic distortion of metals’, *Philosophical Transactions of the Royal Society of London A* **230**, 323 – 362.
- Thakur, D., Ramamoorthy, B. and Vijayaraghavan, L. [2009], ‘Machinability investigation of inconel 718 in high-speed turning’, *The International Journal of Advanced Manufacturing Technology* **45**, 421 – 429.
- Tönshoff, H. [1995], in ‘Spanen’, Springer, Berlin.
- Umbrello, D. [2008], ‘Finite element simulation of conventional and high speed machining of ti6al4v alloy’, *Journal of Material Processing Technology* **196**, 79 – 87.
- Usui, E., Maekawa, K. and Shirakashi, T. [1981], ‘Simulation analysis of built-up edge formation in machining of low carbon steel’, *Bulletin of the Japan Society of Precision Engineering* **15**, 237–242.
- Vaz, M., Owen, D., Kalhori, V., Lundblad, M. and Lindgren, L. [2007], ‘Modelling and simulation of machining processes’, *Archives of Computational Methods in Engineering* **14**, 173 – 204.

- V.Piispanen [1948], ‘Theory of formation of metal chips’, *Journal of Applied Physics* **19**, 876 – 881.
- Wu, W., Jinn, J. and Fischer, C. [2003], Modeling techniques in forming proceses, in G. Dieter and S. S. H.A. Kuhn, eds, ‘Handbook of workability and process design’, ASM International.
- Yen, Y.-C., Jain, A. and Altan, T. [2004], ‘A finite element analysis of orthogonal machining using different tool edge geometries’, *Journal of Materials Processing Technology* **146**, 72 – 81.
- Zerilli, F. and Armstrong, R. [1987], ‘Dislocation-mechanics-based constitutive relations for material dynamics calculations’, *Journal of Applied Physics* **61**, 1816– 1825.
- Zienkiewicz, O. and Taylor, R. [2000], in ‘The finite element method’, Butterworth-Heinemann.
- Zienkiewicz, O. and Zhu, J. [1987], ‘A simple error estimator and adaptive procedure for practical engineering analysis’, *International Journal for Numerical Methods in Engineering* **24**, 337 – 357.
- Zienkiewicz, O. and Zhu, J. [1992], ‘The super convergent patch recovery and a posteriori error estimates. part 1: The recovery technique’, *International Journal for Numerical Methods in Engineering* **33**, 1331 – 1364.
- Zorev, N. [1963], ‘Interrelationship between shear processes occurring along tool face and shear plane in metal cutting’, *International Research in Production Engineering* pp. 42 – 49.
- Zorev, N. [1966], in ‘Metal cutting mechanics’, Pergamon Press, Oxford.